# Tuning the spin-orbit coupling, magnetic proximity, and band hybridization in Fe(001)/MgO/MoS$_2$ multilayers

P. Marcon⬤, R. Arras⬤, D. Li⬤, and L. Calmels⬤[*]

*CEMES, Université de Toulouse, CNRS, 29 rue Jeanne Marvig, F-31055 Toulouse, France*

We present first-principles calculations of the electronic structure and spin texture of a MoS$_2$ monolayer in Fe/MgO/MoS$_2$ multilayers. These metal/insulator/semiconductor stackings are subject to an electron transfer from the Fe layer to the MoS$_2$ sheet, giving rise to a two-dimensional (2D) electron gas, the density of which depends on the MgO layer thickness. We describe the consequences of this electron transfer and of the magnetic proximity effect on the occupation of the conduction bands of the MoS$_2$ layer, on the nature of its band gap, and on the splitting and dispersion of its valence bands near the $\Gamma$ point of the 2D Brillouin zone. The spin splitting and spin texture are reproduced and understood by an effective Hamiltonian, which includes Rashba, Dresselhaus, and Zeeman effects. We finally show that the splitting of the MoS$_2$ valence bands induced near $\Gamma$ by the spin-orbit coupling is rather different when Fe is replaced by a nonmagnetic transition metal such as vanadium.

## I. INTRODUCTION

Transition-metal dichalcogenide (TMDC) monolayers (MLs) are promising two-dimensional (2D) semiconductors that should play a key role in the next generation of electronic, optoelectronic, and spintronic devices. They have already been used as the semiconducting channel of field-effect transistors (FETs), with a carrier mobility higher than that measured in the best Si-based devices and with a large ON-OFF current ratio [1–9]. The possibility of designing complex circuits operating logical operations from TMDC-based FETs has been reported in several articles [10–12]. Their optical properties have also been exploited in different kinds of optoelectronic devices [13], ranging from solar cells [14] to photovoltaic and photodetecting devices [15,16], phototransistors [17–19], photodiodes [14], and light emitting diodes [12]. The use of TMDC layers in spintronic devices has also been considered by different theoretical and experimental teams. Magnetic tunnel junctions (MTJs) based on a nonmagnetic and insulating TMDC spacer and different kinds of magnetic electrodes have thus been studied [20–31]. More complicated stackings have also been considered for spintronic applications, like the Fe/MoS$_2$/phosphorene/Pt multilayer, of which the spin-transfer-torque properties have recently been calculated from first principles [32]. TMDC-based stacks have finally been studied for their possible spin-orbitronics applications. Most of the corresponding studies focused on charge-to-spin conversion at the graphene/TMDC interfaces [33–44], where the TMDC layers are mainly used to provide strong spin-orbit coupling (SOC) effects to the charge carriers supplied by the graphene layer. A large spin-orbit torque effect has also been observed at the TMDC/CoFeB interface, which is potentially interesting for its spin/charge conversion properties [45].

The key role played by TMDC MLs in all these devices is mostly due to the very interesting specificities of their uncommon band structure. Experiments have indeed evidenced that their band gap is direct [46,47]. This has been confirmed by calculations based on first-principles or tight-binding methods, which have shown that the direct band gap occurs at the 6 $K$ points of the first Brillouin zone (BZ) [46]. Calculations have also shown that the combination of the SOC and the lack of inversion symmetry induces a large spin splitting of their valence bands and a smaller but non-negligible spin splitting of their conduction bands at the $K$ valleys [48], with an intimate coupling between the spin and valley degrees of freedom. This coupling splits the six valleys of the TMDC MLs in two degenerated groups with opposite spin splittings, respectively located at the three $K$ and three $K'$ Bloch vectors [49–51]. Absorption of circularly polarized photons has moreover been used to selectively populate the $K$ or $K'$ valleys with electrons and holes [52–55], evidencing that light can be used to perfectly control the TMDC ML valley degree of freedom.

Several authors have further shown that different kinds of external stimuli may be used to control the nature and the energy width of the band gap of a TMDC ML. First-principles calculations have shown, for instance, that a sufficiently large strain can switch the band gap from direct at $K/K'$ to indirect between $\Gamma$ and $K/K'$ [56–62]. A similar switch of the top of the valence band has also been reached by applying an external electric field [63–66], or by creating an interface between the TMDC ML and either an oxide such as EuO [67], or MgO-terminated multilayers [68]. Moreover, different strategies have been investigated for lifting the degeneracy between the bands with opposite spin states located at the $K$ and $K'$ valleys, respectively, starting with the use of an external magnetic field applied perpendicular

[*]lionel.calmels@cemes.fr

to the TMDC layer, thus inducing a Zeeman splitting of the inequivalent valleys [69–75]. Another route, more attractive from the perspective of designing TMDC ML-based devices operating without applying an external magnetic field, has consisted in using interfaces between TMDC and ferromagnetic layers. In this case, the lift of the valley degeneracy is induced by the exchange magnetic field provided by the proximity of the ferromagnet. Different magnetic materials have been considered to reach this aim [20,45,67,76–97]. Interfaces involving covalent bonds between a TMDC layer and a magnetic metal generally fail in preserving the semiconducting character of the TMDC layer [85]. Conversely, these layers remain semiconducting, and their valley degeneracy is generally lifted when they are bound by van der Waals (vdW) interaction, either directly to the magnetic layer or through a single $h$-BN layer intercalated between the TMDC and the ferromagnet [98].

The band structure of a single TMDC layer can finally be modified by the Rashba interaction [99–104], which induces additional lifts of the spin degeneracy near the top of the valence band at $\Gamma$. This occurs for Janus TMDC layers with different kinds of chalcogen atoms on the two sides of the metallic atom layer [105–111], but also when an external electric field is applied perpendicular to a nonpolar TMDC ML [9,64–66,72,75] or to a Janus TMDC layer [108,109]. Last, a Rashba spin splitting of the TMDC valence band near $\Gamma$ has also been observed at the interfaces between a TMDC layer and a Bi surface [112] or at the interface between two different TMDC layers [113]; in these cases, the Rashba effect is due to the interface built-in electric field and to the non-negligible hybridization that occurs across the interface. The spin splitting of the valence bands near $\Gamma$ and the related spin texture induced by Rashba-like SOC effects could allow controlling the spin properties of TMDC-based spin-orbitronics devices with an electric instead of a magnetic field, in particular when the splitting is strong or when the SOC induces a persistent spin texture. Indeed, such a unidirectional spin polarization of the TMDC electron states in the **k**-space should give access to the long carrier spin lifetime required to control the spin orientation [114].

With this scientific and technological context in mind, we have calculated the electronic structure and the magnetic properties of Fe(7MLs)/MgO($n$MLs)/MoS$_2$(1ML) multilayers made of a thin Fe ferromagnetic layer with perpendicular magnetic anisotropy, an insulating MgO layer with a thickness $t_{MgO}$ between 3 and 7 ML, and a single MoS$_2$ layer. Such a stacking, which has recently been synthesized with a 1.5-nm-thick MgO layer [68], allows simultaneously switching the MoS$_2$ band gap (from direct to indirect) and to increase the magnetic proximity effects when the MgO thickness is lowered. Moreover, decreasing the MgO thickness also changes the MgO/MoS$_2$ interface built-in electric field and the subsequent strength of the interface-induced SOC. It finally modifies the energy offset between the MgO and MoS$_2$ bands, possibly leading to different band hybridizations at the MgO/MoS$_2$ interface.

We present a systematic study of the band structure of these multilayers, with a particular focus on the lift of the spin degeneracy and on the spin texture near the valence-band maximum at $\Gamma$, which we have studied as a function of the MgO layer thickness. Our first-principles data are fitted with a simple phenomenological Hamiltonian model that includes exchange Zeeman, Rashba, and Dresselhaus interactions, a possible shift of the valence-band maximum, and a possible modification of the effective mass. We used this model to evaluate the relative weights of the Zeeman, Rashba, and Dresselhaus contributions and understand which of these effects governs the properties of the MoS$_2$ layer, as a function of the MgO thickness. We also show that the model fails at critical MgO thicknesses for which the dispersion of the valence band near $\Gamma$ is governed by band-hybridization between MgO and MoS$_2$, giving rise to persistent spin textures. We finally compare the SOC effects calculated for the Fe/MgO/MoS$_2$ multilayers with those computed for nonmagnetic V/MgO/MoS$_2$ systems.

## II. CALCULATION METHODS

As shown in Fig. 1, we used supercells consisting of asymmetric Fe(7MLs)(001)/MgO(001)/1H-MoS$_2$ multilayers stacked along the $z$ direction and with $t_{MgO}$ between 3 and 7 ML. We only studied multilayers based on the $1H - $MoS$_2$ ML, which is considered the most stable one and is potentially interesting for electronic applications due to its semiconducting behavior (whereas the $1T - $MoS$_2$ phase is metallic). In genuine Fe/MgO/MoS$_2$ samples, the MoS$_2$ layer and the Fe/MgO bilayer both keep their own in-plane lattice parameters, MoS$_2$ being only bound by the weak vdW interaction to the rest of the stacking. Supercells with a perfect matching would contain a huge number of nonequivalent atoms, due to the periodic boundary conditions. Calculating their electronic structure from first principles would be too computationally demanding. As we mainly wish to understand how electron states of the MoS$_2$ single layer are modified by the interface with Fe/MgO, we chose to use orthorhombic-shaped supercells with the lattice parameters $a_1 = a_{MoS_2}$ and $a_2 = \sqrt{3}a_{MoS_2}$, respectively, along the $x$ and $y$ directions. This choice preserves the hexagonal structure and the lattice parameter $a_{MoS_2} = 3.16$ Å calculated for the isolated $1H - $MoS$_2$ sheet at equilibrium, while limiting the number of atoms contained in the supercell. The price to pay is the resulting structural distortion of the Fe/MgO bilayer, which loses its square-shaped aspect leading, in MgO, to a tensile strain of 6.5% along the $x$ axis (where the distance between Mg atoms is stretched from $a_{MgO}/\sqrt{2}$ to $a_1$) and to a compressive strain of $-7.8$% along the $y$ axis (where the distance between second neighbor Mg atoms is compressed from $\sqrt{2}a_{MgO}$ to $a_2$). Strains are also applied to the Fe layer, $a_{Fe}$ being stretched to $a_1$ and $2a_{Fe}$ compressed to $a_2$, respectively, in the $x$ and $y$ directions. We checked that such structural distortions do not drastically change the electronic structure of the bulk Fe and MgO crystals (see Figs. S1 and S2 in the supplemental material [115]). Indeed, even if the distortions split some of the energy bands that would otherwise be degenerated, the density of states (DOS) curves are not drastically changed by the distortions: the Fermi level $E_F$ still crosses the $d$ bands of the Fe crystal and the band gap of MgO. As shown previously [116], the atomic structure with the lowest energy is found when O atoms are located on top of Fe atoms at the
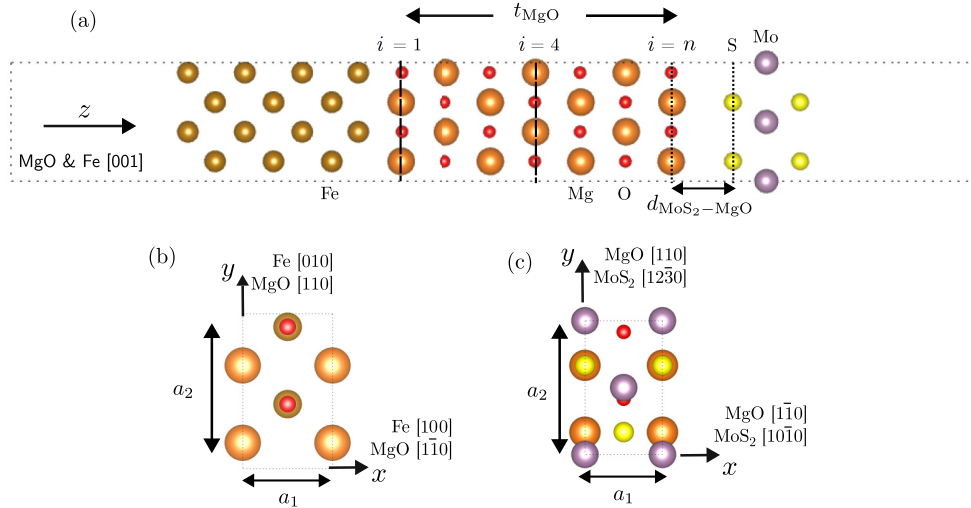
FIG. 1. Atomic structure of the Fe/MgO($n$MLs)/MoS$_2$ supercells: (a) Side view and plane views of (b) the Fe/MgO and (c) MoS$_2$/MgO interfaces.

Fe/MgO interface, while 2/3 of the S atoms are on top of half of the Mg atoms at the MgO/MoS$_2$ interface [68]; see Fig. 1.

A vacuum space of about 16 Å was taken in order to avoid unphysical interactions between two neighboring slabs in the $z$ direction. A dipole correction [117] was added to cancel any spurious electric field created between facing surfaces. Internal coordinates were optimized using a conjugate gradient algorithm, until all forces were less than $10^{-2}$ eV/Å.

First-principles calculations of the physical properties of the Fe/MgO/MoS$_2$ multilayers were performed with the supercells described above and the VASP code [118–121] based on density-functional theory (DFT) and on the projector augmented wave (PAW) method [122]. The energy cutoff was set to 550 eV. All DFT calculations have been done at the Perdew-Burke-Ernzerhof (PBE) level [123]. We also took into account vdW interactions using the Grimme correction [124].

SOC was added self-consistently in electronic structure calculations [125]. The 2D first BZ was sampled with a $20 \times 16 \times 1$ Monkhorst-Pack grid [126] for optimizing the structure and for calculating the DOS curves. Subsequently, the band-structure and spin texture postprocessing were done using the python library PYPROCAR [127].

The built-in electric field in the MgO layers has been estimated from the ratio $|V(z_L) - V(z_R)|/(z_R - z_L)$, where $V(z_L)$ and $V(z_R)$ are the values of the ($xy$)-planar averaged electrostatic potential calculated at the second and penultimate MgO MLs. This method, which should give more reliable results for thicker MgO layers, as it avoids taking into account the sharp variations of the electrostatic potentials at the two interfacial MgO MLs, has been applied to the multilayers with $4 \leqslant t_{\text{MgO}} \leqslant 7$ ML. For the system with $t_{\text{MgO}} = 3$ ML, for which interface effects cannot be avoided, we estimated the electric field at the center of the MgO layers from the values $V(z_L)$ and $V(z_R)$ calculated at the first and third MgO MLs.

Parameters used in the effective Hamiltonian proposed in Sec. III B 3 were fitted from energy bands calculated near the center $\Gamma$ of the BZ and along the $k_x$ or $k_y$ directions, using 30 Bloch wave vectors between $k_{x(y)} = -0.06$ and $+0.06$ Å$^{-1}$.

## III. MgO-THICKNESS DEPENDENCE OF THE ELECTRONIC STRUCTURE AND OF THE SPIN TEXTURE

### A. Overview of the results obtained for Fe/MgO(7MLs)/MoS$_2$

We first briefly summarize and complete the results that we have recently reported for the multilayer with $t_{\text{MgO}} = 7$ ML [68], the largest MgO layer thickness that we will consider here. This system will further be used as a reference when we will describe the increase of the SOC and magnetic proximity effects induced by the decrease of the MgO spacer thickness.

For Fe/MgO(7MLs)/MoS$_2$, the average distance $d_{\text{MoS}_2-\text{MgO}}$ calculated between the interface S and MgO layers [see Fig. 1(a)] is 2.84 Å, a value comparable to that recently reported for the Ga$_2$O$_3$/MoS$_2$ interface [128]. This confirms that the MoS$_2$ layer is bound to the rest of the stacking by weak vdW interaction.

The electronic structure of MoS$_2$ in Fe/MgO(7MLs)/ MoS$_2$ shows strong similarities with that of the isolated MoS$_2$ ML, the overall dispersion of the MoS$_2$ bands being globally preserved in the multilayer, but noticeable differences appear as shown in Fig. 2. In particular, the MoS$_2$ band gap is no longer direct at $K/K'$, but becomes indirect from $\Gamma$ to $K/K'$, due to non-negligible orbital interactions across the MoS$_2$/MgO interface, as will be discussed further on. Moreover, the difference between the work function of the (001) Fe surface (3.95 eV calculated for the surface of the distorted Fe crystal, 4.17 eV measured experimentally [129]) and the electron affinity of MoS$_2$ (4.20 eV according to our calculations, 4.3 eV [130] and 4.7 eV [131] measured in experiments) results in an electron transfer from the Fe/MgO interface to the MoS$_2$ layer, rising $E_{\text{F}}$ above the minimum of the two MoS$_2$ conduction bands with the lowest energy at $K/K'$ (these bands are labeled CB and CB + 1 in Fig. 2).

The transferred electrons occupying these bands form a two-dimensional electron gas (2DEG) with an effective mass of $0.774m_0$ along $\Gamma - K$ ($m_0$ being the mass of the free electron) and an electron density $n_e$ of 0.0543 electron per $\sqrt{3}a^2_{\text{MoS}_2}$ area. This 2DEG is not spin polarized, magnetic
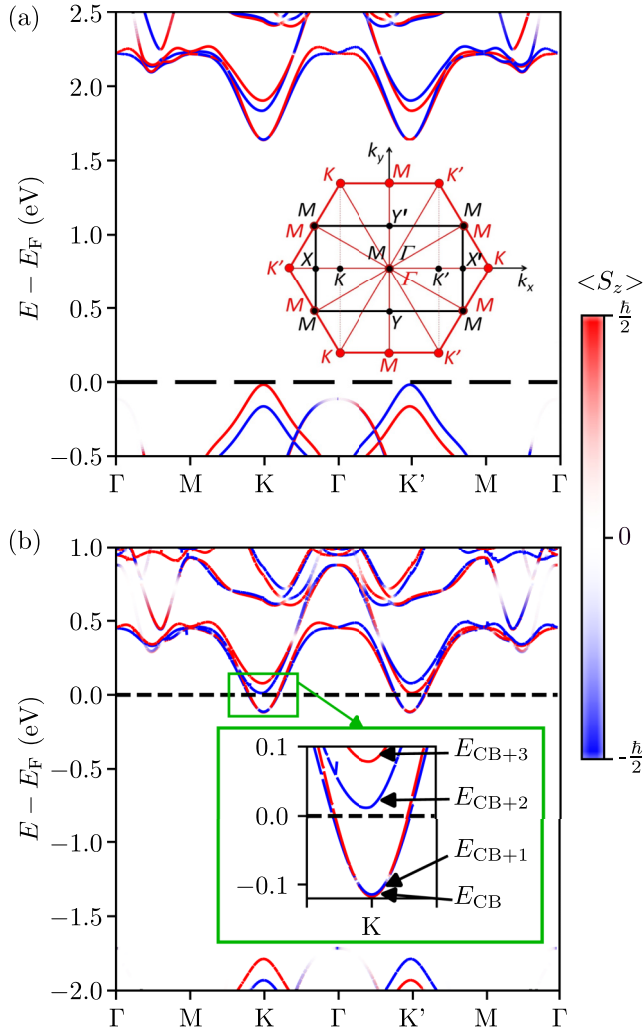
FIG. 2. Spin-projected band structure along the high-symmetry directions of the rectangular BZ of the supercell shown in Fig. 1, for (a) an isolated 1H-MoS$_2$ ML and (b) the MoS$_2$ ML in the Fe/MgO(7MLs)/MoS$_2$ multilayer. The rectangular first BZ of the multilayer is represented in panel (a) with black lines and black letters, where it is compared to the hexagonal BZ of the isolated MoS$_2$ layer (in red).

proximity effects being insufficient to strongly lift the degeneracy between the MoS$_2$ conduction bands with opposite spin directions at $K$ and $K'$. Conduction bands with a higher energy (CB + 2 and CB + 3 in Fig. 2) have their minima at $K/K'$ above $E_F$ for this multilayer. These minima correspond to the conduction-band minima located at the six $Q$-points of the hexagonal primitive-cell BZ of the isolated MoS$_2$ layer (i.e., halfway between $\Gamma$ and $K/K'$). After building the supercell shown in Fig. 1, the minima of CB, CB + 1, CB + 2, and CB + 3 are folded at the same point of the rectangular conventional cell BZ; see Fig. 2.

The charge transferred across the MgO layer creates an internal electric field $E_{\mathrm{int}} = 0.12$ V/Å, which induces Mg-O polar displacements along the [001] direction: we found $\delta z = [\langle z_{\mathrm{Mg}^{2+}} \rangle - \langle z_{\mathrm{O}^{2-}} \rangle] = 0.04$ Å at the center of the MgO layer. This electric field is of the same order of magnitude as the field $\frac{n_e}{\epsilon_r \epsilon_0} = 0.057$ V/Å that would exist in a

capacitor with charge densities $\pm e n_e$ on its plates and a spacer material with the same dielectric constant $\epsilon_r = 9.83$ as that of MgO [132]. This capacitor model, however, assumes a homogeneous spacer material and two-dimensional charge distributions with a negligible thickness compared to $t_{\mathrm{MgO}}$, which should not be the case for the systems with very thin MgO layers that we considered here (this could explain the difference between the values that we calculated and those given by the capacitor model).

Even if magnetic proximity effects are small for the MgO thickness of 7 ML, they are responsible for a significant 0.24 meV spin splitting of the MoS$_2$ valence-band maximum at $\Gamma$. Finally, Fig. 2 shows that the spin direction for electron states near the top of the valence band at $\Gamma$ tilts from out-of-plane for the isolated MoS$_2$ layer to in-plane for MoS$_2$ in Fe/MgO(7MLs)/MoS$_2$.

### B. Tuning the MoS$_2$ electronic structure by decreasing the MgO layer thickness

We now describe the modification of the electronic properties of the MoS$_2$ ML induced by a lowering of the MgO layer thickness, focusing on the MoS$_2$ conduction bands near $K/K'$ and valence bands near $\Gamma$.

#### 1. Occupancy and spin splitting of the MoS$_2$ conduction bands at K/K'

The electron density $n_e$ of the 2DEG transferred from the Fe electrode to the MoS$_2$ ML has been calculated by integrating the Mo- and S-atom partial charge densities corresponding to the occupied part of CB, CB + 1, and CB + 2. Figure 3(a) shows that $n_e$ monotonously increases from 0.0543 to 0.0963 electron per $\sqrt{3}a_{\mathrm{MoS}_2}^2$ area, when the MgO-layer thickness decreases from 7 to 3 ML. This increase is mainly due to the pulling down below $E_F$ of the minimum of the conduction band CB + 2. This can be seen in Fig. 3(b), where we plotted the energy of the conduction-band minima of CB, CB + 1, CB + 2, and CB + 3 as a function of the MgO layer thickness. The energy shift induced by a lowering of the MgO layer thickness is not rigid: The energy (with respect to $E_F$) of the minimum of the conduction bands CB and CB + 1 and the number of electrons populating these two bands are nearly independent of $t_{\mathrm{MgO}}$. On the other hand, the energy of the CB + 2 and CB + 3 conduction-band minima tends to decrease (and the population of CB + 2 to increase) when the thickness of the MgO layer is lowered.

As explained in Sec. III A, an internal electric field $E_{\mathrm{int}}$ appears in the MgO dielectric layer due to the electron transfer from the Fe electrode to the MoS$_2$ ML. The value of $E_{\mathrm{int}}$ calculated at the center of the MgO layer is represented in Fig. 3(c) as a function of the MgO layer thickness. It increases from 0.12 V/Å for $t_{\mathrm{MgO}} = 7$ ML to 0.24 V/Å for $t_{\mathrm{MgO}} = 3$ ML, and the variation of $E_{\mathrm{int}}$ with the MgO-layer thickness is more or less proportional to $n_e$, as would be the case for the simple capacitor model.

The Mg-O buckling $\delta z$ is represented in Fig. 3(d) as a function of the MgO atomic layer index $i$ and for $t_{\mathrm{MgO}} = 3$–7 ML. Except at the Fe/MgO interface, this buckling is positive, which corresponds to the expected displacement of the Mg cations in the direction of the internal electric field (i.e.,
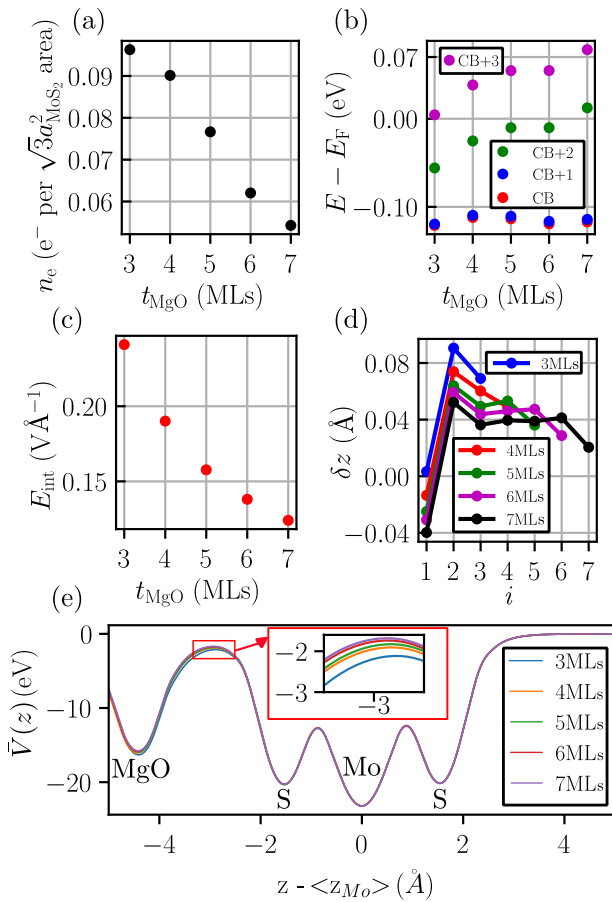
FIG. 3. (a) Electron density $n_e$ of the 2DEG occupying the conduction bands of the MoS$_2$ layer, vs the MgO layer thickness. (b) Energy of the successive conduction-band minima at $K/K'$, vs MgO layer thickness. (c) Internal electric field $E_{int}$ at the center of the MgO layer, vs MgO layer thickness. (d) Mg-O buckling $\delta z$ vs index $i$ of the MgO atomic layer ($i = 1$ corresponding to the MgO ML at the Fe/MgO interface) and for different thicknesses of the MgO layer. (e) ($xy$)-planar averaged electrostatic potential in the vicinity of the MoS$_2$ ML, as a function of the $z$ coordinate and for different values of the MgO layer thickness (the inset shows the values of the potential in the vdW gap at the MgO/MoS$_2$ interface).

towards MoS$_2$) and of the O anions in the opposite direction (towards Fe). The value of the buckling at the center of the MgO layer increases with the internal electric field, from 0.04 Å for $t_{MgO} = 7$ ML to 0.09 Å for $t_{MgO} = 3$ ML.

The difference between the $xy$-planar averaged electrostatic potentials $\overline{V}(z)$ calculated near the MoS$_2$ layers of multilayers with different values of the MgO thickness is very small, except in the vdW gap between the top MgO and interface S atomic layers, as shown in Fig. 3(e). As will be explained later, the associated increase of the electric field in the vdW gap will be responsible for the enhancement of the SOC effects.

We finally turn our attention to the effects of the MgO layer thickness on the spin splitting of the conduction bands mostly induced by SOC at each of the $K$ and $K'$ valleys, and on the valley Zeeman splitting induced between the $K$ and $K'$ valleys by magnetic proximity effects. The spin splitting of the
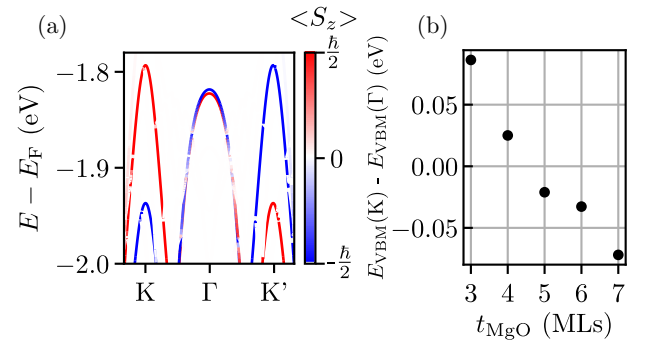


FIG. 4. (a) Contribution of the MoS$_2$ ML to the highest-energy valence bands of Fe/MgO(4MLs)/MoS$_2$. (b) Energy difference between the top of the valence bands at $K$ and $\Gamma$, as a function of the MgO layer thickness.

conduction bands decreases from 3 meV for $t_{MgO} = 7$ ML (a value close to that reported in Ref. [50] for the isolated MoS$_2$ layer) to 1.6 meV for $t_{MgO} = 3$ ML. The valley Zeeman splitting of the conduction bands is of 0.6 meV for $t_{MgO} = 3$ ML, i.e., for the thickness at which the magnetic proximity effects are the strongest; this value corresponds to an effective magnetic field of a few Tesla. It becomes negligible and difficult to accurately calculate for thicker MgO layers. It may be too small to be measured experimentally.

### 2. Nature of the MoS$_2$ band gap

The switchover of the MoS$_2$ band gap, from direct (at $K/K'$) for an isolated MoS$_2$ layer to indirect (from $\Gamma$ to $K/K'$) for a MoS$_2$ ML in a Fe/MgO/MoS$_2$ multilayer, occurs above a critical MgO layer thickness. Figure 4(a) shows the dispersion of the MoS$_2$ valence bands for $t_{MgO} = 4$ ML, the largest MgO thickness for which the band gap of MoS$_2$ is direct. The difference between the energies of the valence-band maxima (VBM) calculated at $K/K'$ and at $\Gamma$ is plotted in Fig. 4(b) as a function of the MgO layer thickness: it is negative for $t_{MgO} \geqslant 5$ ML, from which the band gap becomes indirect. This is mainly due to a 0.16 eV decrease of the energy difference $[E_{CBM}(K/K') - E_{VBM}(\Gamma)]$ between the conduction-band minimum (CBM) at $K/K'$ and the VBM at $\Gamma$, when $t_{MgO}$ increases from 3 to 7 ML, while the energy difference $[E_{CBM}(K/K') - E_{VBM}(K/K')]$ is nearly independent of the MgO layer thickness. These observations are not surprising: the top of the valence band at $\Gamma$ mainly involves Mo-$d_{z^2}$ and S-$p_z$ atomic orbitals, the latter being very sensitive to the presence of neighboring atomic layers (i.e., to the thickness of the MgO layer), while the CBM and VBM at $K/K'$ do not involve contributions from $S - p_z$ atomic orbitals.

Several interdependent driving forces can be cited to explain that the contribution of the $p_z$ orbitals of the interface S atoms and the energy of the MoS$_2$ VBM at $\Gamma$ change with $t_{MgO}$. First, the energy (and the number) of the MgO valence bands depends on the thickness of the MgO layer, in particular when it becomes ultrathin. Furthermore, the energy of the MgO bands is also shifted by the internal electric field induced in all the MgO atomic layers by the charge transfer from Fe to MoS$_2$. Finally, as we will discuss below, a hybridization between Mo, S, Mg, and O atomic orbitals occurs when the
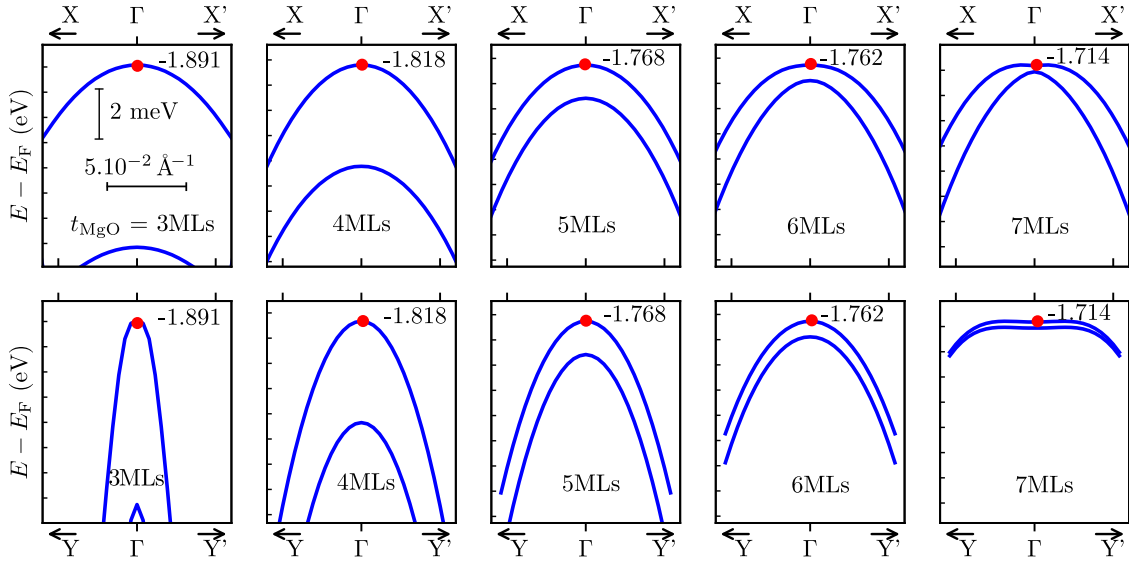
FIG. 5. Dispersion of the $MoS_2$ valence bands near the VBM at $\Gamma$, calculated from first principles for Bloch wave vectors along the $\Gamma$-$X$ direction (upper panels) and along the $\Gamma$-$Y$ direction (lower panels). The different panels correspond to Fe/MgO/MoS$_2$ multilayers with $t_{MgO} = 3, 4, 5, 6$, and 7 ML. The energy of the VBM at $\Gamma$ (indicated by a red dot) is given in each panel.

MgO and $MoS_2$ valence bands have similar energies. These arguments suggest that changes in the $MoS_2$ VBM at $\Gamma$ are more likely to be due to thickness-dependent interactions with MgO bands than to a modification of the width of the vdW gap, which stays nearly constant, around 2.85 Å (except maybe for $t_{MgO} = 3$ MLs, for which it slightly decreases down to 2.8 Å).

### 3. Splitting and dispersion of the valence bands near $\Gamma$

Figure 5 shows the dispersion near the top of the $MoS_2$ valence bands at $\Gamma$, calculated for Fe/MgO($n$MLs)/MoS$_2$ multilayers with different MgO layer thicknesses. The two bands in this figure are splitted by the SOC and magnetic proximity effects. The dispersion and band splitting computed along $\Gamma$-$X$ are similar to those calculated from a simple model of a 2DEG immersed in a perpendicular exchange magnetic field and with Rashba-like SOC. Indeed, the top panels of Fig. 5 corresponding to $t_{MgO} = 7$ ML and to $t_{MgO} = 3$–6 ML, respectively, are similar to those displayed in Refs. [104,133–136] for a Zeeman effect smaller than SOC effects, and in Refs. [134,136] for SOC effects smaller than the Zeeman one.

Figure 5 shows that the spin splitting induced at $\Gamma$ by the exchange magnetic field continuously increases when the MgO-layer thickness decreases, from 0.24 meV for $t_{MgO} = 7$ ML to 7.2 meV for $t_{MgO} = 3$ ML. This splitting could be measured by angle-resolved photoemission spectroscopy (ARPES), providing that spectra can be recorded with a sufficient resolution. Figure 5 also shows that the dispersion of the valence bands is not isotropic, with a band curvature bigger along $\Gamma$-$Y$ than along $\Gamma$-$X$ (two different effective masses $m_x^*$ and $m_y^*$ are necessary to describe the dispersion). This anisotropy is a consequence of the anisotropy of the structure of the MgO/MoS$_2$ interface [see Fig. 1(c)], where the hexagonal $MoS_2$ and the rectangular top MgO MLs are juxtaposed.

The valence-band dispersion and spin slitting are different for $t_{MgO} = 7$ and 3 ML than for $t_{MgO} = 4, 5$, and 6 ML.

Indeed, Fig. 5 shows that the valence bands become unexpectedly flat along $\Gamma$-$Y$ for $t_{MgO} = 7$ ML. For $t_{MgO} = 3$ ML, the $MoS_2$ ML actually contributes to four different electron bands instead of two, in a small energy range of 26 meV near the top of the valence bands at $\Gamma$; only the two bands with the lowest energy and the highest $MoS_2$ contributions are shown in Fig. 5. We will see in the next section that the specific band dispersion observed for $t_{MgO} = 3$ and 7 ML is a consequence of the hybridization and interaction between the valence bands of $MoS_2$ and of MgO.

We used an effective Hamiltonian to reproduce the band structure, considering that the splitting near $\Gamma$ of the highest energy valence bands has two main sources: (i) the SOC which manifests itself, in this system with broken inversion symmetry, through a combination of the Rashba and Dresselhaus effects, and (ii) the Zeeman effect due to the proximity of the Fe ferromagnetic layer. To estimate the relative contributions of the Rashba, Dresselhaus, and Zeeman effects, we fitted the band structure near the top of the valence bands at $\Gamma$ computed from first principles, with the eigenvalues that we calculated for an effective Hamiltonian taking all these effects into account [137,138]. This Hamiltonian is given by

$$\hat{H} = \hat{H}_0 + \hat{H}_R + \hat{H}_D + \hat{H}_Z, \tag{1}$$

where

$$\hat{H}_0 = \epsilon\hat{I} + \frac{\hat{p}_x{}^2}{2m_x^*} + \frac{\hat{p}_y{}^2}{2m_y^*} \tag{2}$$

describes a free 2DEG with a nonisotropic dispersion ($m_x^*$ and $m_y^*$ are the effective masses, respectively, along the $x$ and $y$ directions, $\hat{I}$ is the identity matrix, and $\epsilon$ is an offset energy). Because of the nontrivial crystal structure of the slabs and interfaces described here, the little point group associated with $\Gamma$ is $C_s$, which only possesses two symmetry elements: the identity and a (100) mirror plane. Several nonequivalent terms, invariant by this small number of symmetry

elements, could contribute to the SOC effect in a Hamiltonian model. Considering the splitting of the valence bands near Γ, we have chosen to approximate the SOC part of the Hamiltonian by only keeping the terms corresponding to the standard two-dimensional linear Rashba and Dresselhaus interactions [100,137,139]:

$$\hat{H}_R = \alpha(k_y\hat{\sigma}_x - \hat{\sigma}_y k_x) \tag{3}$$

and

$$\hat{H}_D = \beta(k_y\hat{\sigma}_x + \hat{\sigma}_y k_x). \tag{4}$$

$\hat{H}_R$ and $\hat{H}_D$ depend on the $x$ and $y$ components of the Pauli matrix $\hat{\sigma}$ and wave vector **k**. $\alpha$ and $\beta$ are, respectively, the 2D Rashba and Dresselhaus coefficients. We further demonstrate that these two terms, respectively induced by the built-in electric field due to charge reorganization near the MgO/MoS$_2$ interface and by the $xy$-crystalline anisotropy of this interface, indeed suffice to describe most of the consequences of SOC calculated from first principles, thus gathering the most important physical elements necessary to explain the properties of Fe/MgO/MoS$_2$ multilayers. We checked that cubic SOC terms are negligible for small Bloch-vector ranges near Γ [140]. The Zeeman term, which accounts for magnetic proximity effects, is given by

$$\hat{H}_Z = \mu_B B\hat{\sigma}_z, \tag{5}$$

where $B$ is the modulus of the effective exchange magnetic field oriented along the $z$ axis. We have restricted our description of the Hamiltonian to these few contributions only, which correctly account for the small wave-vector dependence of the MoS$_2$ valence-band spin splitting near Γ for $4 \leqslant t_{MgO} \leqslant$ 6 ML, as the MoS$_2$ valence bands neither hybridize nor strongly interact with MgO bands in this case. The effective Hamiltonian would be more complicated out of this MgO thickness range: It should contain more terms to go beyond the simple parabolic dispersion and include the description of both the MoS$_2$ and MgO hybridized bands, which is beyond the scope of the present article.

The diagonalization of $\hat{H}$ gives access to the dispersion of the splitted bands:

$$E_\pm = \epsilon + \frac{\hbar^2 k_x^2}{2m_x^*} + \frac{\hbar^2 k_y^2}{2m_y^*}$$
$$\pm \sqrt{(\alpha - \beta)^2 k_x^2 + (\alpha + \beta)^2 k_y^2 + (\mu_B B)^2}. \tag{6}$$

Table I gives the value of the parameters $\epsilon$, $m_x^*$, $m_y^*$, $\alpha$, $\beta$, and $\mu_B B$ obtained by fitting the energies of the MoS$_2$ band structures calculated from first principles near the top of the valence band at Γ with Eq. (6). This table shows that the SOC coefficients ($\alpha$ and $\beta$) and the exchange Zeeman proximity effect ($\mu_B B$) all increase when the MgO thickness decreases. The spin splitting calculated at Γ ($2\mu_B B = 4$ meV for $t_{MgO} = 4$ ML) is due to the exchange effect induced by the proximity of the ferromagnetic layer and of the tail of its spin-polarized electron wave functions, which decreases exponentially in the thin MgO layer. $\beta$ is always larger than $\alpha$ (however, this latter is never negligible). The spin-orbit coefficients $\alpha$ and $\beta$ that we calculated have the same order of magnitude as the Rashba coefficient computed for a single

TABLE I. Parameters of the effective Hamiltonian fitted from the MoS$_2$ band structure and spin texture calculated from first principles near the top of the valence bands at Γ, for Fe/MgO/MoS$_2$ multilayers with $t_{MgO} = 4$, 5, and 6 ML.

| $t_{MgO}$ | 4 ML | 5 ML | 6 ML |
|---|---|---|---|
| $\epsilon$ (eV) | −1.82 | −1.77 | −1.76 |
| $m_x^*/m_0$ | −3.542 | −3.263 | −3.121 |
| $m_y^*/m_0$ | −1.191 | −1.475 | −2.35 |
| $\alpha$ (meVÅ) | 11.27 | 3.98 | −5.07 |
| $\beta$ (meVÅ) | 22.34 | 18.23 | 13.95 |
| $\mu_B B$ (meV) | 2.0 | 0.66 | 0.31 |

MoS$_2$ layer in a perpendicular electric field of 0.1 V/Å [64]. However, such a Hamiltonian model is not suitable to describe the band structure for multilayers with $t_{MgO} = 3$ and 7 ML, hybridization effects being stronger in these cases, as will be discussed in the next section.

The comparison between the first-principles results and the analytical equations corresponding to the Hamiltonian model is shown in Appendix A.

#### 4. Hybridization of the valence bands near Γ

The contributions to the band structure of the MoS$_2$ and of its first-neighbor MgO MLs are compared in Fig. 6, with an energy scale larger than in Fig. 5 (the splitting near the top of the MoS$_2$ valence bands discussed in Sec. III B 3 is not visible at this scale). This figure explains why the MoS$_2$ valence bands show a different dispersion along Γ-Y and Γ-X: this is mostly due to the presence of MgO bands, which are more dispersive along Γ-Y than along Γ-X. Due to this stronger dispersion, the highest energy MoS$_2$ valence bands and MgO surface bands do overlap along Γ-Y, displaying an anticrossing that locally affects the dispersion of the MoS$_2$ bands.

The highest-energy interface-MgO bands shift downwards when $t_{MgO}$ decreases. This is partly due to the value of the potential jump between the Fe/MgO and the MgO/MoS$_2$ interfaces, which is found smaller for thinner than for thicker MgO layers, despite higher values of the electric field in the MgO layer. The interface MgO band reaches the MoS$_2$ valence-band maximum at Γ for $t_{MgO} = 3$ ML, giving rise to a strong hybridization near Γ, between the two splitted MoS$_2$ valence bands and two (one for each spin state) MgO bands.

A second MgO band can finally be observed at lower energies in this figure. Although the interface MgO ML contributes less to this band (which only appears as a light line in Fig. 6), its presence slightly modifies the dispersion of the MoS$_2$ valence bands for $t_{MgO} = 7$ ML. For this MgO-layer thickness, the difference between the energies of the MgO and MoS$_2$ bands becomes smaller near Γ, and the MoS$_2$ bands lose their parabolic shape, in particular along Γ-Y, due to orbital interactions across the vdW gap.

#### 5. Spin texture of the MoS$_2$ valence bands near Γ

This section describes the Bloch-vector and MgO-thickness dependences of the direction of the spin vector, for the two highest-energy valence bands shown in Fig. 5.
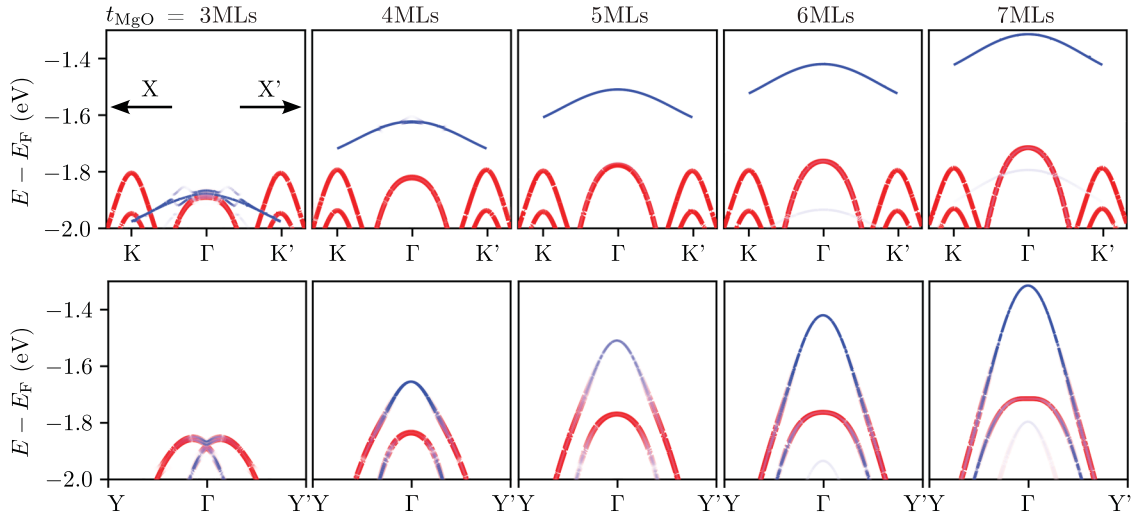
FIG. 6. Contributions of the MgO interface ML (blue lines) and of the MoS$_2$ ML (red lines) to the valence bands of the Fe/MgO/MoS$_2$ multilayers, for $t_{MgO}$ = 3, 4, 5, 6, and 7 ML and for Bloch wave vectors along the $\Gamma$-$X$ (upper panels) and $\Gamma$-$Y$ (lower panels) directions. The $K/K'$ points are located between $\Gamma$ and the $X/X'$ points.

We only describe the spin texture of the multilayers with $t_{MgO}$ = 4, 5, 6, and 7 ML.

Figure 7 shows the variations of the angle $\theta$ between the spin vector and the $z$ axis, calculated for the two highest energy-splitted MoS$_2$ valence bands, for small Bloch vectors along $\Gamma$-$X$ and $\Gamma$-$Y$ and for different values of the MgO layer thickness. The spin, for these two valence bands, is always perpendicular to the MoS$_2$ layer at the center $\Gamma$ of the BZ ($\theta = 0$ or $\pi$). The component of the spin vector perpendicular to the MoS$_2$ layer decreases when the Bloch vector increases along $\Gamma$-$X$ (see the top panels in Fig. 7), at the benefit of its in-plane projection. This rotation of the spin from mostly out-of-plane at $\Gamma$ to mostly in-plane far from $\Gamma$ occurs at smaller Bloch vectors for the thicker MgO layers. This is due to the fact that

magnetic proximity effects, which tend to align the spin either parallel or antiparallel to the exchange magnetic field (i.e., along the $z$ direction), increase when the MgO-layer thickness decreases. Conversely, the built-in electric field induced by electronic reorganizations in the vdW gap and the related SOC effects tend to lay the spin in-plane and dominate magnetic proximity effects for thicker MgO layers. The variations of $\theta$ along $\Gamma$-$Y$ (bottom panels in Fig. 7) show similar behavior for all the MgO-layer thicknesses, except $t_{MgO}$ = 7 ML for which it does not vary monotonously with $|k_y|$, due to the interaction with the lowest energy MgO band (shown as a light line in Fig. 6).

Figure 8 shows the modulus and direction of the in-plane projection of the spin vector, calculated for the highest energy
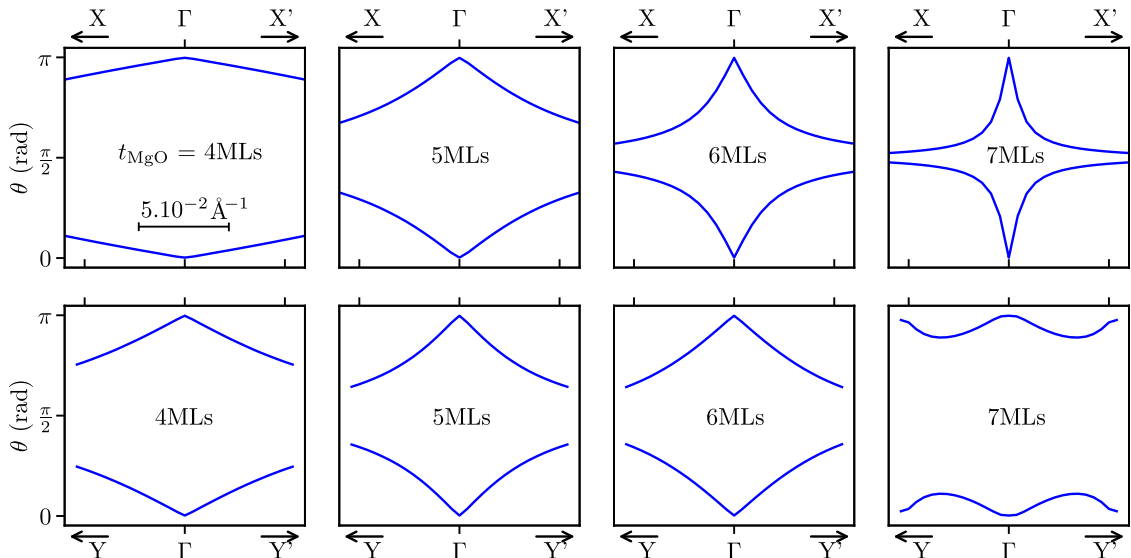


FIG. 7. Angle $\theta$ between the spin vector and the stacking axis, calculated from first principles and plotted near the top of the MoS$_2$ valence bands located at $\Gamma$, for Fe/MgO/MoS$_2$ multilayers with $t_{MgO}$ = 4, 5, 6, and 7 ML and for Bloch wave vectors along the $\Gamma$-$X$ (upper panels) and $\Gamma$-$Y$ (lower panels) directions.
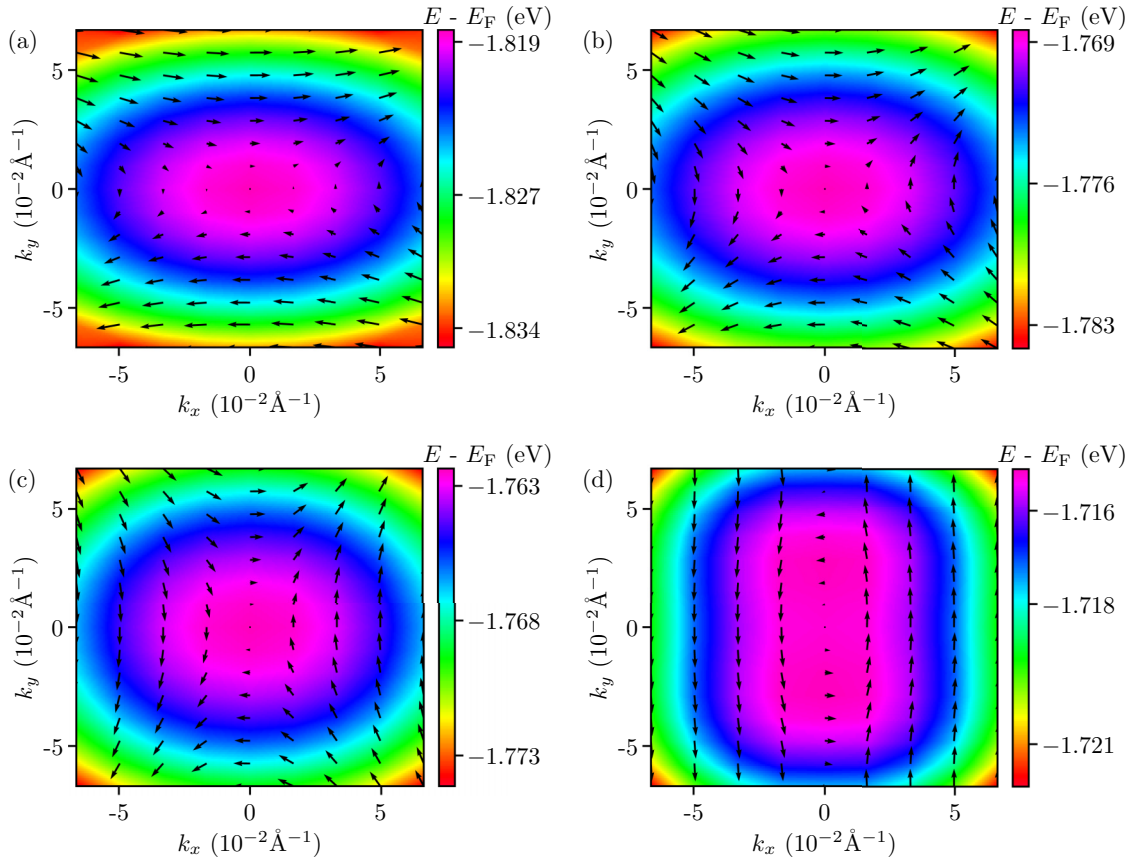
FIG. 8. Modulus and direction of the in-plane projection of the spin vector calculated near $\Gamma$ from first principles, for the highest energy valence band of MoS$_2$ in Fe/MgO/MoS$_2$ multilayers with $t_{\text{MgO}} = 4$ ML (a), 5 ML (b), 6 ML (c) and 7 ML (d).

MoS$_2$ valence band shown in Fig. 5, drawn for several values of the MgO layer thickness and as a function of $k_x$ and $k_y$. The ellipsoidal shape of the constant energy lines displayed by the panels corresponding to $t_{\text{MgO}} = 4$, 5, and 6 ML is mostly due to the anisotropy of the MgO/MoS$_2$ interface (which would also exist if the Fe/MgO bilayer would not be distorted). This ellipsoidal shape only disappears at the MgO layer thicknesses for which hybridization or interactions occur between MgO and MoS$_2$ bands. The spin texture computed for the multilayer Fe/MgO(5MLs)/MoS$_2$ is characteristic of that previously calculated [137,141–145] for a 2DEG subjected to a Dresselhaus interaction [146,147]. The spin texture is more complicated for $t_{\text{MgO}} = 4$ and 6 ML, for which Rashba and Dresselhaus interactions may both contribute. It becomes very particular for $t_{\text{MgO}} = 7$ ML. In this latter case, the spin vector mostly points towards the $y$ direction. Previous studies have shown that such a nearly persistent spin texture can occur in a 2D electron gas with the $C_{2v}$ symmetry, when the Rashba and Dresselhaus interactions have comparable intensities [137,141,142,144]. Things are more complicated for Fe/MgO/MoS$_2$ multilayers with the $C_s$ symmetry: In this case, the SOC should involve more terms than the simple Rashba and Dresselhaus interactions. These two latter contributions only dominate when hybridization/interaction between MoS$_2$ and MgO bands is weak, which is not the case for the MgO thicknesses for which a persistent spin texture is found; additional SOC terms accounting for the MgO/MoS$_2$

hybridization should be considered in this case. Persistent spin textures are important for spintronic applications because they could give rise to an infinite spin lifetime [148,149].

We have obtained similar spin textures for the second of the two highest energy splitted MoS$_2$ valence bands at $\Gamma$, but with an opposite direction of the in-plane projection of the spin vector.

The direction of the spin vector computed for these two bands from first-principles (Figs. 7 and 8) can be compared to the spin texture calculated analytically using the Hamiltonian model described in Sec. III B 3. The eigenvectors with energies $E_\pm$ can be used to obtain the angles $\theta_\pm$ (angle between the $z$ axis and the spin vector) and $\phi_\pm$ (angle between the $x$ axis and the projection of the spin vector in the $xy$ plane) which give the direction of the spin vector for these two states. These angles are given by

$$\theta_+ = \arctan\left\{\frac{\sqrt{(\alpha - \beta)^2 k_x^2 + (\alpha + \beta)^2 k_y^2}}{\mu_B B}\right\},$$
$$\theta_- = \pi - \theta_+, \tag{7}$$

and

$$\tan(\phi_+) = \frac{(\beta - \alpha)k_x}{(\beta + \alpha)k_y}, \quad \phi_- = \pi + \phi_+. \tag{8}$$
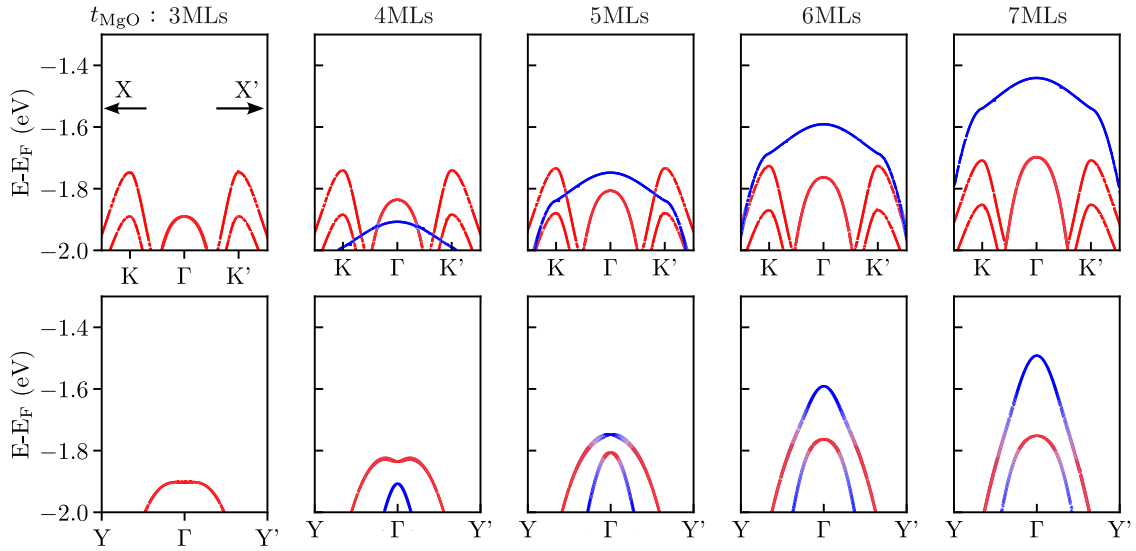
FIG. 9. Contributions of the MgO interface ML (blue lines) and of the MoS$_2$ ML (red lines) to the valence bands of the V/MgO/MoS$_2$ multilayers, for $t_{MgO} = 3, 4, 5, 6,$ and 7 ML and for Bloch wave vectors along the $\Gamma$-$X$ (upper panels) and along the $\Gamma$-$Y$ (lower panels) directions. The $K/K'$ points are located between $\Gamma$ and the $X/X'$ points.

The good agreement between the spin-texture calculated from first-principles and the values of $\theta_\pm$ and $\phi_\pm$ obtained using the effective Hamiltonian is shown in Appendix A and confirms the validity of the model.

## IV. COMPARISON WITH THE NONMAGNETIC V/MgO/MoS$_2$ MULTILAYERS

We compare the results obtained for Fe/MgO($n$MLs)/MoS$_2$ multilayers with the band structure and spin texture calculated for V/MgO($n$MLs)/MoS$_2$ systems, using the same first-principles method, V being a nonmagnetic 3$d$ transition metal with an atomic number (23) close to that of Fe (26). V/MgO/MoS$_2$ multilayers thus allow us to study the MgO-thickness dependence of SOC effects in a MoS$_2$-based stacking free of any exchange Zeeman interaction.

The dispersion of the MoS$_2$ valence bands is described for $t_{MgO} = 3$–7 ML, first in a figure with a relatively large energy scale (Fig. 9), where the interfacial MgO bands are also shown. The dispersion along $\Gamma$-$X$ shows that a MgO band crosses the MoS$_2$ valence bands, as for the Fe/MgO/MoS$_2$ multilayers. However, this crossing occurs for thicker MgO layers in the V/MgO/MoS$_2$ stacking ($t_{MgO} < 5$ MLs) than in the Fe/MgO/MoS$_2$ multilayers ($t_{MgO} \leqslant 3$ MLs), the energy difference between the top of the MoS$_2$ and MgO valence bands being smaller for V/MgO/MoS$_2$ than for Fe/MgO/MoS$_2$. Figure 10, which uses a smaller energy scale for $t_{MgO} = 5$–7 ML, shows that the two MoS$_2$ valence bands are degenerate at $\Gamma$. The spin splitting out of $\Gamma$ is proportional to the modulus of the Bloch vector, as expected for a nonmagnetic two-dimensional system with a Rashba or a Dresselhaus SOC. Even for multilayers with $t_{MgO} \geqslant 5$ ML, for which hybridization effects are expected to be smaller, this spin splitting is not trivial: it increases for Bloch vectors along $\Gamma$-$X$ and decreases along $\Gamma$-$Y$, when $t_{MgO}$ increases from 5 to 7 ML (see Fig. 10).

The valence-band splitting shown in Fig. 10 can be fitted by an effective Hamiltonian similar to that [Eq. (1)] used for studying Fe/MgO/MoS$_2$, but without the Zeeman term.

The parameters $\epsilon$, $m_x^*$, $m_y^*$, $\alpha$, and $\beta$ for which the best agreement is found between $E_\pm$ and the dispersion near $\Gamma$ of the MoS$_2$ valence bands calculated from first principles are given in Table II for the V/MgO/MoS$_2$ multilayers with $t_{MgO} = 5, 6,$ and 7 ML (thicknesses for which the Hamiltonian model can be used). This table shows that the Rashba and
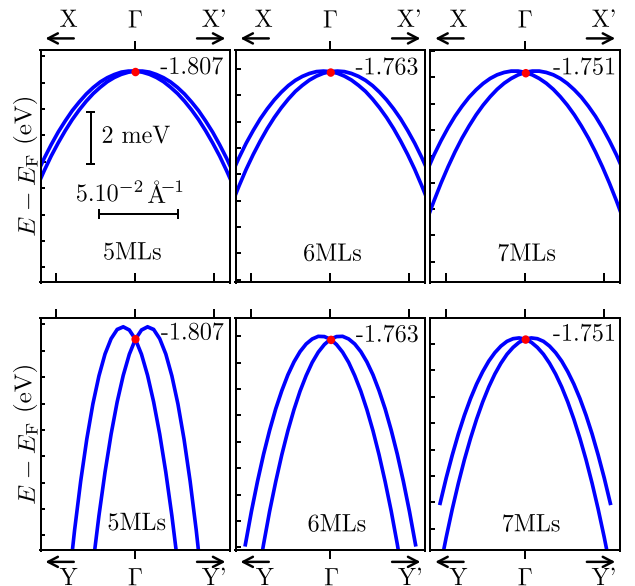


FIG. 10. Dispersion of the MoS$_2$ valence bands near the VBM at $\Gamma$, calculated from first principles for Bloch wave vectors along the $\Gamma$-$X$ direction (upper panels) and along the $\Gamma$-$Y$ direction (lower panels). The different panels correspond to V/MgO/MoS$_2$ multilayers with $t_{MgO} = 5, 6,$ and 7 ML. The energy of the VBM at $\Gamma$ (indicated by a red dot) is given in each panel.

TABLE II. Parameters of the effective Hamiltonian achieving the best possible agreement with the MoS$_2$ band structure and spin texture calculated from first principles near the top of the valence bands at $\Gamma$, for V/MgO/MoS$_2$ multilayers with $t_{MgO} = 5$, 6, and 7 ML.

| $t_{MgO}$ | 5 ML | 6 ML | 7 ML |
|---|---|---|---|
| $\epsilon$ (eV) | $-1.81$ | $-1.76$ | $-1.71$ |
| $m_x^*/m_0$ | $-3.584$ | $-3.263$ | $-3.175$ |
| $m_y^*/m_0$ | $-0.495$ | $-1.111$ | $-1.492$ |
| $\alpha$ (meVÅ) | 57.3 | 14.3 | 2.86 |
| $\beta$ (meVÅ) | 61.9 | 24.67 | 21.43 |
| $(\beta - \alpha)$ (meVÅ) | 4.6 | 10.37 | 18.57 |
| $(\beta + \alpha)$ (meVÅ) | 119.2 | 38.97 | 24.29 |

Dresselhaus parameters are greater than those calculated for the Fe/MgO/MoS$_2$ multilayers and that both increase when the MgO layer thickness decreases. $(\beta - \alpha)$ decreases while $(\beta + \alpha)$ increases when the MgO layer thickness decreases. This explains why the linear band splitting increases along $\Gamma$-$X$ and decreases along $\Gamma$-$Y$ when $t_{MgO}$ increases from 5 to 7 ML. The band dispersion along these two directions is indeed given by

$$E_{\pm} = \epsilon + \frac{\hbar^2 k_x^2}{2m_x^*} \pm |(\beta - \alpha)k_x| \qquad (9)$$

along $\Gamma$-$X$ and by

$$E_{\pm} = \epsilon + \frac{\hbar^2 k_y^2}{2m_y^*} \pm |(\beta + \alpha)k_y| \qquad (10)$$

along $\Gamma$-$Y$.

We have finally calculated the spin texture near the top of the valence bands of MoS$_2$ in V/MgO/MoS$_2$ multilayers with $t_{MgO} = 4$–7 ML (see Figs. S3 and S4 in the supplemental material [115]). As expected, the spin vector is entirely in the MoS$_2$ plane, and the spin texture for the multilayers with $t_{MgO} = 6$ and 7 ML (for which hybridization with MgO is small) is characteristic of that of a 2DEG with Dresselhaus interaction. As for Fe/MgO/MoS$_2$ multilayers, we found that the spin texture changes drastically for MgO thicknesses for which the MgO bands approach or cross the MoS$_2$ valence bands, giving rise to a nearly persistent spin texture for $t_{MgO} = 4$ ML. The persistent spin texture obtained for $t_{MgO} = 5$ ML is mainly due to the fact that $\alpha \approx \beta$ for this MgO thickness.

## V. DISCUSSION

We must discuss the robustness of our main results and whether they would stay valid in multilayers free of any structural distortion. The increase of the SOC parameters $\alpha$ and $\beta$ when the MgO layer thickness decreases and the corresponding Dresselhaus + Rashba-like spin texture are mostly due to the electric potential drop across the MoS$_2$ ML, resulting from the charge transfer in the Fe/MgO/MoS$_2$ and V/MgO/MoS$_2$ multilayers, as clearly shown in Fig. 11. These charge-transfer-induced effects would also exist without structural distortion of the MgO layer, the electron transfer being mostly due (if we ignore interface effects) to the
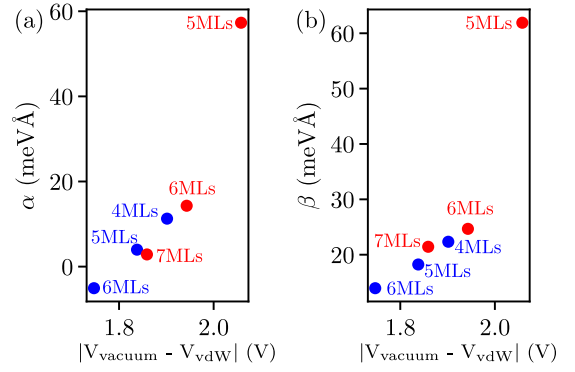


FIG. 11. Values of the SOC parameters $\alpha$ and $\beta$, vs the electric potential drop $|V_{vacuum} - V_{vdW}|$ calculated between the vacuum and the center of the vdW gap for Fe/MgO/MoS$_2$ (blue dots) and V/MgO/MoS$_2$ (red dots) multilayers, for different values of $t_{MgO}$.

difference between the metal work function and MoS$_2$ electron affinity, which would keep similar values without distorting MgO [68].

Let us now focus on Fe/MgO/MoS$_2$ magnetic multilayers. The increase of the spin splitting near the maximum of the MoS$_2$ valence bands at $\Gamma$ and the increase of the $z$ component of the spin textures when the thickness of the MgO layer decreases would be preserved without distortion of the MgO layer, as it is only due to the increase of the magnetic proximity effects when the MgO spacer becomes thinner.

Fe/MgO/MoS$_2$ multilayers free of any distortion should thus keep being considered as versatile and adjustable systems in which the SOC and magnetic proximity effects can continuously be tuned by a judicious choice of the MgO layer thickness.

However, although the electronic structure of the MgO layer does not globally change when it is distorted (the width of its band gap being nearly the same with and without distortion; see Fig. S2 in the supplementary material [115]), the details of the dispersion of the MgO bands along the $\Gamma$-$X$ and $\Gamma$-$Y$ directions are slightly modified by the crystal distortion, as can be seen in Appendix B. This may have consequences on those physical properties of the MoS$_2$ ML that depend on the interactions or hybridization between the MgO and MoS$_2$ valence bands, as we have seen in Sec. III B 4. In particular, the critical MgO thicknesses below which the MgO bands cross the MoS$_2$ valence bands should be the same along the $\Gamma$-$X$ and $\Gamma$-$Y$ directions for genuine Fe/MgO/MoS$_2$ samples. This may slightly change the MgO thickness range where the Hamiltonian model applies, but the existence of such a MgO range is not questioned.

Finally, the persistent spin textures that we have observed for specific MgO thicknesses may also be due to the splitting of the MgO bands near $\Gamma$ and to their different dispersion along $\Gamma$-$X$ and $\Gamma$-$Y$: The persistent spin texture may disappear in Fe/MgO/MoS$_2$ multilayers (but may remain in the V/MgO/MoS$_2$ systems with the MgO thickness for which similar values of $\alpha$ and $\beta$ have been found) without distorting the MgO layer. However, our results clearly show that using alternative metallic/insulating bilayers with a different band dispersion of the insulating layer along $\Gamma$-$X$ and $\Gamma$-$Y$, and an

insulator thickness such that the insulator valence bands cross those of the $MoS_2$ ML, should be considered as a promising avenue to stabilize persistent spin textures in a $MoS_2$ ML. This would confirm that the interface symmetry can promote persistent spin textures, following symmetry arguments previously used to stabilize a persistent spin texture in a bulk crystal [150,151].

## VI. SUMMARY

We have investigated the electronic and magnetic properties of a $MoS_2$ ML in Fe(001)/MgO($n$MLs)/$MoS_2$(1ML) stacks with $n = 3–7$. In these multilayers, the $MoS_2$ ML is only bound by weak vdW interaction to the Fe/MgO bilayer. An electron transfer occurs from Fe to $MoS_2$ in these multilayers, due to the difference between the Fe work function and $MoS_2$ electron affinity. We have demonstrated that the density of the corresponding 2DEG (with negligible spin-polarization) and the resulting built-in electric field in the MgO layer increase when the MgO layer thickness decreases. We have studied the splitting of the $MoS_2$ valence bands near $\Gamma$ for these multilayers: This splitting is due to the interplay of various magnetic interactions, namely the Rashba, Dresselhaus, and Zeeman interactions. Their contributions are understood by an analytical Hamiltonian model. The coefficients describing the spin-orbit and exchange-Zeeman interactions increase when the MgO layer thickness decreases, with a Dresselhaus term that dominates the Rashba one for the thinner MgO layers. As long as the $MoS_2$ valence bands do not interact with those of MgO, these coefficients explain the details of the dispersion, the spin texture, and the rotation of the spin vector near $\Gamma$, from mostly in-plane to mostly out-of-plane when the MgO layer thickness decreases. Fe/MgO/$MoS_2$ multilayers with ultrathin MgO layers (1 or 2 ML) have not been considered here. They would also warrant being studied (provided that they can be grown with a high-quality crystal structure), as they should show stronger magnetic proximity effects; hybridization between the MgO, $MoS_2$, and even Fe bands should dominate in this case. Additionally, we compared the results obtained for the magnetic Fe/MgO/$MoS_2$ multilayers with those calculated for nonmagnetic V/MgO/$MoS_2$ systems, which show a different dispersion of the $MoS_2$ valence bands and only an in-plane spin texture, due to the absence of Zeeman effects in this case.

Van der Waals insulators such as hexagonal BN could be used instead of MgO to get thinner insulating layers between Fe and $MoS_2$, thus increasing the magnetic proximity effects. We finally suggest that a persistent spin texture could emerge in metal/insulator/TMDC multilayers based on an insulating layer other than MgO but with an anisotropic band dispersion and a thickness for which the insulator valence bands cross those of the $MoS_2$ monolayer.
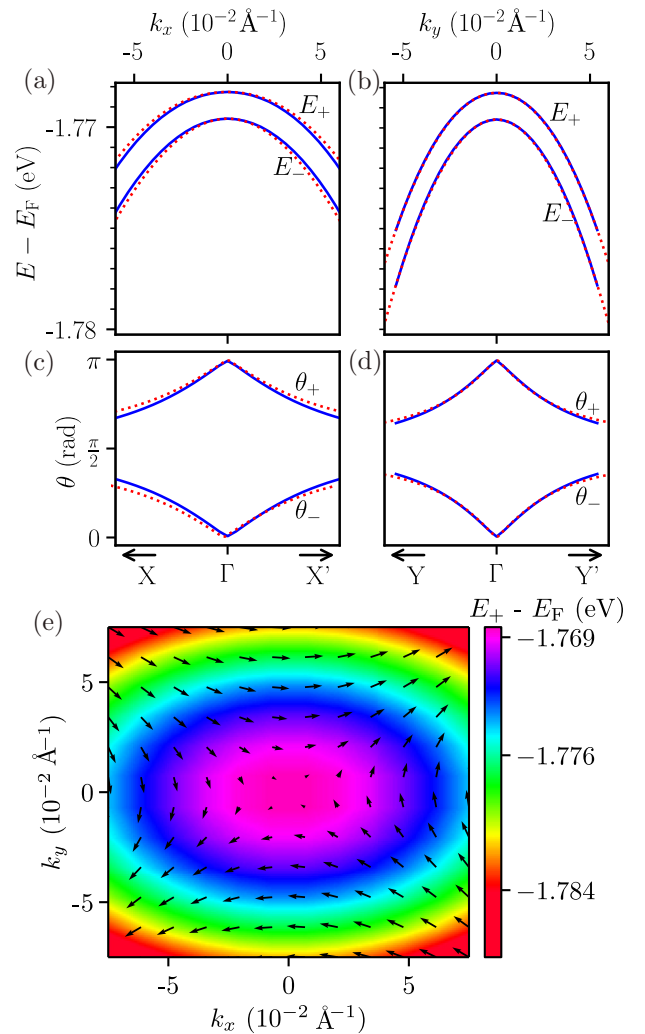
FIG. 12. (a) Dispersion of the highest-energy $MoS_2$ valence bands of the multilayer Fe/MgO(5MLs)/$MoS_2$, for Bloch vectors along $\Gamma$-$X$; the blue solid lines correspond to the first-principles data, while the red dotted lines correspond to the eigenvalues $E_+$ and $E_-$ of the effective Hamiltonian. (b) Same as (a), but for Bloch vectors along $\Gamma$-$Y$. (c) Angle $\theta$ between the spin vector and the $z$ axis, calculated for the multilayer Fe/MgO(5MLs)/$MoS_2$ and for Bloch vectors along $\Gamma$-$X$; the blue solid lines correspond to the first-principles data and the red dotted lines to the angles $\theta_+$ and $\theta_-$ calculated from the eigenvectors of the effective Hamiltonian. (d) Same as (c), but for Bloch vectors along $\Gamma$-$Y$. (e) Modulus and direction of the in-plane projection of the spin vector, calculated for the multilayer Fe/MgO(5MLs)/$MoS_2$ using the angle $\phi_+$ [Eq. (8)].

## APPENDIX A: DFT VERSUS EFFECTIVE HAMILTONIAN

Figures 12(a) and 12(b) compare the dispersion of the splitted $MoS_2$ valence bands calculated from first principles for the multilayer Fe/MgO(5MLs)/$MoS_2$, respectively, for Bloch wave vectors along the $\Gamma$-$X$ and $\Gamma$-$Y$ directions of the first BZ, with the energies $E_\pm$ fitted with the set of parameters given in Table I. Figures 12(c) and 12(d) compare the values of the angle $\theta$ calculated from first principles for these two bands of the same multilayer, with the angles $\theta_\pm$ calculated from Eq. (7) and the same set of parameters. Figure 12(e) finally
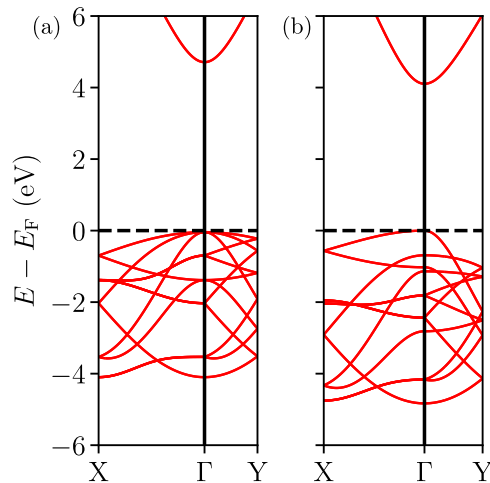
FIG. 13. Bulk MgO band structure calculated along the $\Gamma$-$X$ and $\Gamma$-$Y$ directions, for (a) the nondistorted cubic crystal and (b) the distorted crystal.

shows the modulus and direction of the projection of the spin vector in the $xy$-plane, calculated for Fe/MgO(5MLs)/MoS$_2$, using the angle $\phi_+$ given in Eq. (8) and the parameters $\alpha$ and $\beta$ previously obtained for this multilayer. All these figures show that the effective Hamiltonian correctly describes the results calculated from first principles.

Similar comparisons are given in the supplemental material for Fe/MgO(4MLs)/MoS$_2$ and Fe/MgO(6MLs)/

MoS$_2$ (Figs. S5–S8 in [115]), and for V/MgO/MoS$_2$ multilayers with $t_{MgO}$ = 5, 6, and 7 MLs (Figs. S9–S14 in [115]).

## APPENDIX B: MgO BAND STRUCTURE IN THE $\Gamma$-$X$ AND $\Gamma$-$Y$ DIRECTIONS: CUBIC VERSUS DISTORTED BULK CRYSTALS

In this Appendix, we compare the dispersion of the bands calculated for bulk MgO along the $\Gamma$-$X$ and $\Gamma$-$Y$ directions of the Brillouin zone of a conventional quadratic unit cell, when the distortion described in Sec. II is taken into account and when this distortion does not occur (cubic MgO crystal with the rocksalt structure). The distortion makes the [110] and [1$\bar{1}$0] MgO crystallographic axes nonequivalent, which lifts the degeneracy between MgO bands that would otherwise be degenerated at $\Gamma$ (see Fig. 13). After this degeneracy has been lifted, the MgO valence band which has the highest energy near $\Gamma$ has a stronger dispersion along $\Gamma$-$Y$ than along $\Gamma$-$X$: this band corresponds to that drawn with a blue line in Figs. 6 and 9. The band that has been splitted from the former one by the structural distortion is found just below it (see Fig. 13); it shows a stronger dispersion along $\Gamma$-$X$ than along $\Gamma$-$Y$. Without any distortion, these two bands are degenerate at $\Gamma$ and both a dispersive band and a less dispersive one are found, with similar energies along the $\Gamma$-$X$ and $\Gamma$-$Y$ directions.

The band structure calculated for the distorted bulk MgO crystal explains the difference between the dispersions of the MgO valence bands calculated at the MgO/MoS$_2$ interface, along $\Gamma$-$X$ and along $\Gamma$-$Y$.

[1] V. Podzorov, M. E. Gershenson, Ch. Kloc, R. Zeis, and E. Bucher, Appl. Phys. Lett. **84**, 3301 (2004).

[2] B. Radisavljevic, A. Radenovic, J. Brivio, V. Giacometti, and A. Kis, Nat. Nanotechnol. **6**, 147 (2011).

[3] L. Liu, S. B. Kumar, Y. Ouyang, and J. Guo, IEEE Trans. Electron Dev. **58**, 3042 (2011).

[4] Y. Yoon, K. Ganapathi, and S. Salahuddin, Nano Lett. **11**, 3768 (2011).

[5] H. Fang, S. Chuang, T. C. Chang, K. Takei, T. Takahashi, and A. Javey, Nano Lett. **12**, 3788 (2012).

[6] D. Lembke and A. Kis, ACS Nano **6**, 10070 (2012).

[7] Q. H. Wang, K. Kalantar-Zadeh, A. Kis, J. N. Coleman, and M. S. Strano, Nat. Nanotechnol. **7**, 699 (2012).

[8] S. Das, R. Gulotty, A. V. Sumant, and A. Roelofs, Nano Lett. **14**, 2861 (2014).

[9] J. Kang, W. Liu, and K. Banerjee, Appl. Phys. Lett. **104**, 093106 (2014).

[10] B. Radisavljevic, M. B. Whitwick, and A. Kis, ACS Nano **5**, 9934 (2011).

[11] H. Wang, L. Yu, Y.-H. Lee, Y. Shi, A. Hsu, M. L. Chin, L.-J. Li, M. Dubey, J. Kong, and T. Palacios, Nano Lett. **12**, 4674 (2012).

[12] P. J. Jeon, J. S. Kim, J. Y. Lim, Y. Cho, A. Pezeshki, H. S. Lee, S. Yu, S.-W. Min, and S. Im, ACS Appl. Mater. Interfaces **7**, 22333 (2015).

[13] H. Wang, C. Li, P. Fang, Z. Zhang, and J. Z. Zhang, Chem. Soc. Rev. **47**, 6101 (2018).

[14] W. Liu, X. Yang, Y. Zhang, M. Xu, and H. Chen, RSC Adv. **4**, 32744 (2014).

[15] G. Wang, L. Bouet, M. M. Glazov, T. Amand, E. L. Ivchenko, E. Palleau, X. Marie, and B. Urbaszek, 2D Mater. **2**, 034002 (2015).

[16] T. A. Shastry, I. Balla, H. Bergeron, S. H. Amsterdam, T. J. Marks, and M. C. Hersam, ACS Nano **10**, 10573 (2016).

[17] H. S. Lee, S.-W. Min, Y.-G. Chang, M. K. Park, T. Nam, H. Kim, J. H. Kim, S. Ryu, and S. Im, Nano Lett. **12**, 3695 (2012).

[18] Z. Yin, H. Li, H. Li, L. Jiang, Y. Shi, Y. Sun, G. Lu, Q. Zhang, X. Chen, and H. Zhang, ACS Nano **6**, 74 (2012).

[19] J. Miao, W. Hu, Y. Jing, W. Luo, L. Liao, A. Pan, S. Wu, J. Cheng, X. Chen, and W. Lu, Small **11**, 2392 (2015).

[20] K. Dolui, A. Narayan, I. Rungger, and S. Sanvito, Phys. Rev. B **90**, 041401(R) (2014).

[21] H.-C. Wu, C. Ó. Coileáin, M. Abid, O. Mauit, A. Syrlybekov, A. Khalid, H. Xu, R. Gatensby, J. Jing Wang, H. Liu, L. Yang, G. S. Duesberg, H.-Z. Zhang, M. Abid, and I. V. Shvets, Sci. Rep. **5**, 15984 (2015).

[22] W. Wang, Y. Liu, L. Tang, Y. Jin, T. Zhao, and F. Xiu, Sci. Rep. **4**, 6928 (2015).

[23] M. Z. Iqbal, M. W. Iqbal, S. Siddique, M. F. Khan, and S. M. Ramay, Sci. Rep. **6**, 21038 (2016).

[24] H. Zhang, M. Ye, Y. Wang, R. Quhe, Y. Pan, Y. Guo, Z. Song, J. Yang, W. Guo, and J. Lu, Phys. Chem. Chem. Phys. **18**, 16367 (2016).

[25] W. C. Wong, S. M. Ng, H. F. Wong, C. L. Mak, and C. W. Leung, IEEE Trans. Magn. **53**, 1 (2017).

[26] A. Dankert, P. Pashaei, M. V. Kamalakar, A. P. S. Gaur, S. Sahoo, I. Rungger, A. Narayan, K. Dolui, M. A. Hoque, R. S. Patel, M. P. de Jong, R. S. Katiyar, S. Sanvito, and S. P. Dash, ACS Nano **11**, 6389 (2017).

[27] K. Zhao, Y. Xing, J. Han, J. Feng, W. Shi, B. Zhang, and Z. Zeng, J. Magn. Magn. Mater. **432**, 10 (2017).

[28] M. F. Khan, H. Kim, G. Nazir, S. Jung, and J. Eom, Nanoscale **10**, 16703 (2018).

[29] A. Kumar and S. Choudhary, J. Supercond. Nov. Magn. **31**, 3245 (2018).

[30] W. Rotjanapittayakul, W. Pijitrojana, T. Archer, S. Sanvito, and J. Prasongkit, Sci. Rep. **8**, 4779 (2018).

[31] H. Lin, F. Yan, C. Hu, Q. Lv, W. Zhu, Z. Wang, Z. Wei, K. Chang, and K. Wang, ACS Appl. Mater. Interfaces **12**, 43921 (2020).

[32] S. K. Behera and P. Deb, Phys. Chem. Chem. Phys. **22**, 19139 (2020).

[33] A. Avsar, J. Y. Tan, T. Taychatanapat, J. Balakrishnan, G. Koon, Y. Yeo, J. Lahiri, A. Carvalho, A. S. Rodin, E. O'Farrell, G. Eda, A. H. Castro Neto, and B. Özyilmaz, Nat. Commun. **5**, 4875 (2014).

[34] M. Gmitra and J. Fabian, Phys. Rev. B **92**, 155403 (2015).

[35] Z. Wang, D.-K. Ki, J. Y. Khoo, D. Mauro, H. Berger, L. S. Levitov, and A. F. Morpurgo, Phys. Rev. X **6**, 041020 (2016).

[36] W. Yan, O. Txoperena, R. Llopis, H. Dery, L. E. Hueso, and F. Casanova, Nat. Commun. **7**, 13372 (2016).

[37] M. Offidani, R. Milletarì, R. Raimondi, and A. Ferreira, Phys. Rev. Lett. **119**, 196801 (2017).

[38] J. H. Garcia, A. W. Cummings, and S. Roche, Nano Lett. **17**, 5078 (2017).

[39] A. Dankert and S. P. Dash, Nat. Commun. **8**, 16093 (2017).

[40] M. Gmitra and J. Fabian, Phys. Rev. Lett. **119**, 146401 (2017).

[41] S. Omar and B. J. van Wees, Phys. Rev. B **95**, 081404(R) (2017).

[42] T. S. Ghiasi, A. A. Kaverzin, P. J. Blah, and B. J. van Wees, Nano Lett. **19**, 5959 (2019).

[43] C. K. Safeer, J. Ingla-Aynés, F. Herling, J. H. Garcia, M. Vila, N. Ontoso, M. R. Calvo, S. Roche, L. E. Hueso, and F. Casanova, Nano Lett. **19**, 1074 (2019).

[44] B. Zhao, D. Khokhriakov, Y. Zhang, H. Fu, B. Karpiak, A. M. Hoque, X. Xu, Y. Jiang, B. Yan, and S. P. Dash, Phys. Rev. Res. **2**, 013286 (2020).

[45] Q. Shao, G. Yu, Y.-W. Lan, Y. Shi, M.-Y. Li, C. Zheng, X. Zhu, L.-J. Li, P. K. Amiri, and K. L. Wang, Nano Lett. **16**, 7514 (2016).

[46] A. Splendiani, L. Sun, Y. Zhang, T. Li, J. Kim, C.-Y. Chim, G. Galli, and F. Wang, Nano Lett. **10**, 1271 (2010).

[47] K. F. Mak, C. Lee, J. Hone, J. Shan, and T. F. Heinz, Phys. Rev. Lett. **105**, 136805 (2010).

[48] Z. Y. Zhu, Y. C. Cheng, and U. Schwingenschlögl, Phys. Rev. B **84**, 153402 (2011).

[49] D. Xiao, G.-B. Liu, W. Feng, X. Xu, and W. Yao, Phys. Rev. Lett. **108**, 196802 (2012).

[50] K. Kosmider, J. W. Gonzalez, and J. Fernandez-Rossier, Phys. Rev. B **88**, 245436 (2013).

[51] X. Xu, W. Yao, D. Xiao, and T. F. Heinz, Nat. Phys. **10**, 343 (2014).

[52] H. Zeng, J. Dai, W. Yao, D. Xiao, and X. Cui, Nat. Nanotechnol. **7**, 490 (2012).

[53] K. F. Mak, K. He, J. Shan, and T. F. Heinz, Nat. Nanotechnol. **7**, 494 (2012).

[54] T. Cao, G. Wang, W. Han, H. Ye, C. Zhu, J. Shi, Q. Niu, P. Tan, E. Wang, B. Liu, and J. Feng, Nat. Commun. **3**, 887 (2012).

[55] H. Yuan, X. Wang, B. Lian, H. Zhang, X. Fang, B. Shen, G. Xu, Y. Xu, S.-C. Zhang, H. Y. Hwang, and Y. Cui, Nat. Nanotechnol. **9**, 851 (2014).

[56] T. Li, Phys. Rev. B **85**, 235407 (2012).

[57] Q. Yue, J. Kang, Z. Shao, X. Zhang, S. Chang, G. Wang, S. Qin, and J. Li, Phys. Lett. A **376**, 1166 (2012).

[58] Q. Zhang, Y. Cheng, L.-Y. Gan, and U. Schwingenschlögl, Phys. Rev. B **88**, 245447 (2013).

[59] H. Shi, H. Pan, Y.-W. Zhang, and B. I. Yakobson, Phys. Rev. B **87**, 155304 (2013).

[60] L. Wang, A. Kutana, and B. I. Yakobson, Ann. Phys. **526**, L7 (2014).

[61] M. A. U. Absor, H. Kotaka, F. Ishii, and M. Saito, Phys. Rev. B **94**, 115131 (2016).

[62] R. K. Defo, S. Fang, S. N. Shirodkar, G. A. Tritsaris, A. Dimoulas, and E. Kaxiras, Phys. Rev. B **94**, 155310 (2016).

[63] N. Zibouche, P. Philipsen, T. Heine, and A. Kuc, Phys. Chem. Chem. Phys. **16**, 11251 (2014).

[64] C. Cheng, J.-T. Sun, X.-R. Chen, H.-X. Fu, and S. Meng, Nanoscale **8**, 17854 (2016).

[65] Y. Affandi, M. A. U. Absor, and K. Abraha, J. Phys.: Conf. Ser. **1011**, 012070 (2018).

[66] Y. Affandi and M. A. Ulil Absor, Physica E **114**, 113611 (2019).

[67] Q. Zhang, S. A. Yang, W. Mi, Y. Cheng, and U. Schwingenschlögl, Adv. Mater. **28**, 959 (2016).

[68] Z. Zhou, P. Marcon, X. Devaux, P. Pigeat, A. Bouché, S. Migot, A. Jaafar, R. Arras, M. Vergnat, L. Ren, H. Tornatzky, C. Robert, X. Marie, J.-M. George, H.-Y. Jaffrès, M. Stoffel, H. Rinnert, Z. Wei, P. Renucci, L. Calmels *et al.*, ACS Appl. Mater. Interfaces **13**, 32579 (2021).

[69] Y. Li, J. Ludwig, T. Low, A. Chernikov, X. Cui, G. Arefe, Y. D. Kim, A. M. van der Zande, A. Rigosi, H. M. Hill, S. H. Kim, J. Hone, Z. Li, D. Smirnov, and T. F. Heinz, Phys. Rev. Lett. **113**, 266804 (2014).

[70] A. Kormányos, V. Zólyomi, N. D. Drummond, and G. Burkard, Phys. Rev. X **4**, 011034 (2014).

[71] D. MacNeill, C. Heikes, K. F. Mak, Z. Anderson, A. Kormányos, V. Zólyomi, J. Park, and D. C. Ralph, Phys. Rev. Lett. **114**, 037401 (2015).

[72] K. V. Shanavas and S. Satpathy, Phys. Rev. B **91**, 235145 (2015).

[73] G. Aivazian, Z. Gong, A. M. Jones, R.-L. Chu, J. Yan, D. G. Mandrus, C. Zhang, D. Cobden, W. Yao, and X. Xu, Nat. Phys. **11**, 148 (2015).

[74] A. Srivastava, M. Sidler, A. V. Allain, D. S. Lembke, A. Kis, and A. Imamoğlu, Nat. Phys. **11**, 141 (2015).

[75] A. Kuc and T. Heine, Chem. Soc. Rev. **44**, 2603 (2015).

[76] L.-Y. Gan, Q. Zhang, Y. Cheng, and U. Schwingenschlögl, Phys. Rev. B **88**, 235310 (2013).

[77] Q. Chen, Y. Ouyang, S. Yuan, R. Li, and J. Wang, ACS Appl. Mater. Interfaces **6**, 16835 (2014).

[78] N. Feng, W. Mi, Y. Cheng, Z. Guo, U. Schwingenschlögl, and H. Bai, ACS Appl. Mater. Interfaces **6**, 4587 (2014).

[79] M. Yin, X. Wang, W. Mi, and B. Yang, Comput. Mater. Sci. **99**, 326 (2015).

[80] J. Qi, X. Li, Q. Niu, and J. Feng, Phys. Rev. B **92**, 121403(R) (2015).

[81] Y. Ye, J. Xiao, H. Wang, Z. Ye, H. Zhu, M. Zhao, Y. Wang, J. Zhao, X. Yin, and X. Zhang, Nat. Nanotechnol. **11**, 598 (2016).

[82] O. L. Sanchez, D. Ovchinnikov, S. Misra, A. Allain, and A. Kis, Nano Lett. **16**, 5792 (2016).

[83] B. Liu, L.-J. Wu, Y.-Q. Zhao, L.-Z. Wang, and M.-Q. Cai, Eur. Phys. J. B **89**, 80 (2016).

[84] D. Zhong, K. L. Seyler, X. Linpeng, R. Cheng, N. Sivadas, B. Huang, E. Schmidgall, T. Taniguchi, K. Watanabe, M. A. McGuire, W. Yao, D. Xiao, K.-M. C. Fu, and X. Xu, Sci. Adv. **3**, e1603113 (2017).

[85] T. Garandel, R. Arras, X. Marie, P. Renucci, and L. Calmels, Phys. Rev. B **95**, 075402 (2017).

[86] K.-A. Min, J. Cha, K. Cho, and S. Hong, 2D Mater. **4**, 024006 (2017).

[87] D. Somvanshi, S. Kallatt, C. Venkatesh, S. Nair, G. Gupta, J. K. Anthony, D. Karmakar, and K. Majumdar, Phys. Rev. B **96**, 205423 (2017).

[88] Y. Song, X. Wang, and W. Mi, Adv. Electron. Mater. **3**, 1700245 (2017).

[89] C. Zhao, T. Norden, P. Zhang, P. Zhao, Y. Cheng, F. Sun, J. P. Parry, P. Taheri, J. Wang, Y. Yang, T. Scrace, K. Kang, S. Yang, G.-x. Miao, R. Sabirianov, G. Kioseoglou, W. Huang, A. Petrou, and H. Zeng, Nat. Nanotechnol. **12**, 757 (2017).

[90] X. Xue, X. Wang, and W. Mi, J. Phys. D **52**, 115303 (2019).

[91] T. Norden, C. Zhao, P. Zhang, R. Sabirianov, A. Petrou, and H. Zeng, Nat. Commun. **10**, 4163 (2019).

[92] C. Lin, Y. Li, Q. Wei, Q. Shen, Y. Cheng, and W. Huang, ACS Appl. Mater. Interfaces **11**, 18858 (2019).

[93] M. Ge, Y. Su, H. Wang, G. Yang, and J. Zhang, RSC Adv. **9**, 14766 (2019).

[94] K. Zollner, P. E. Faria Junior, and J. Fabian, Phys. Rev. B **100**, 085128 (2019).

[95] J. Xie, L. Jia, H. Shi, D. Yang, and M. Si, Jpn. J. Appl. Phys. **58**, 010906 (2019).

[96] D. Zhong, K. L. Seyler, X. Linpeng, N. P. Wilson, T. Taniguchi, K. Watanabe, M. A. McGuire, K.-M. C. Fu, D. Xiao, W. Yao, and X. Xu, Nat. Nanotechnol. **15**, 187 (2020).

[97] Y. Zhang, K. Shinokita, K. Watanabe, T. Taniguchi, M. Goto, D. Kan, Y. Shimakawa, Y. Moritomo, T. Nishihara, Y. Miyauchi, and K. Matsuda, Adv. Mater. **32**, 2003501 (2020).

[98] K. Zollner, P. E. Faria Junior, and J. Fabian, Phys. Rev. B **101**, 085112 (2020).

[99] E. Rashba and F. T. Tela, Solid State **2**, 1224 (1960).

[100] Y. A. Bychkov and E. I. Rashba, J. Phys. C **17**, 6039 (1984).

[101] A. Manchon, H. C. Koo, J. Nitta, S. M. Frolov, and R. A. Duine, Nat. Mater. **14**, 871 (2015).

[102] G. Bihlmayer, O. Rader, and R. Winkler, New J. Phys. **17**, 050202 (2015).

[103] H. W. Yeom and M. Grioni, J. Electron Spectrosc. Relat. Phenom. **201**, 2 (2015).

[104] G. Bihlmayer, P. Noël, D. V. Vyalikh, E. V. Chulkov, and A. Manchon, Nat. Rev. Phys. **4**, 642 (2022).

[105] Y. C. Cheng, Z. Y. Zhu, M. Tahir, and U. Schwingenschlögl, Europhys. Lett. **102**, 57001 (2013).

[106] Q.-F. Yao, J. Cai, W.-Y. Tong, S.-J. Gong, J.-Q. Wang, X. Wan, C.-G. Duan, and J. H. Chu, Phys. Rev. B **95**, 165401 (2017).

[107] M. A. U. Absor, I. Santoso, Harsojo, K. Abraha, H. Kotaka, F. Ishii, and M. Saito, J. Appl. Phys. **122**, 153905 (2017).

[108] M. Adhib Ulil Absor, H. Kotaka, F. Ishii, and M. Saito, Jpn. J. Appl. Phys. **57**, 04FP01 (2018).

[109] T. Hu, F. Jia, G. Zhao, J. Wu, A. Stroppa, and W. Ren, Phys. Rev. B **97**, 235404 (2018).

[110] J. Chen, K. Wu, H. Ma, W. Hu, and J. Yang, RSC Adv. **10**, 6388 (2020).

[111] P. A. L. Sino, L.-Y. Feng, R. A. B. Villaos, H. N. Cruzado, Z.-Q. Huang, C.-H. Hsu, and F.-C. Chuang, Nanoscale Adv. **3**, 6608 (2021).

[112] K. Lee, W. S. Yun, and J. D. Lee, Phys. Rev. B **91**, 125420 (2015).

[113] L. Xiang, Y. Ke, and Q. Zhang, Appl. Phys. Lett. **115**, 203501 (2019).

[114] J. Schliemann and D. Loss, Phys. Rev. B **68**, 165311 (2003).

[115] See Supplemental Material at http://link.aps.org/supplemental/10.1103/PhysRevB.109.155403 for additional details on: the band structure of the distorted bulk Fe and MgO crystals; the spin-textures calculated from first principles for V/MgO/MoS$_2$ multilayers; the comparison between the valence band energies calculated from first principles and from the model Hamiltonian, both for Fe/MgO/MoS$_2$ and V/MgO/MoS$_2$ multilayers; the spin textures calculated from the model Hamiltonian for Fe/MgO/MoS$_2$ and V/MgO/MoS$_2$ multilayers; the comparison between the spin texture calculated from first principles and from the model Hamiltonian for Fe/MgO/MoS$_2$ multilayers.

[116] T. Urano and T. Kanaji, J. Phys. Soc. Jpn. **57**, 3403 (1988).

[117] J. Neugebauer and M. Scheffler, Phys. Rev. B **46**, 16067 (1992).

[118] G. Kresse and J. Hafner, Phys. Rev. B **47**, 558 (1993).

[119] G. Kresse and J. Hafner, Phys. Rev. B **49**, 14251 (1994).

[120] G. Kresse and J. Furthmüller, Comput. Mater. Sci. **6**, 15 (1996).

[121] G. Kresse and J. Furthmüller, Phys. Rev. B **54**, 11169 (1996).

[122] P. E. Blöchl, Phys. Rev. B **50**, 17953 (1994).

[123] J. P. Perdew, K. Burke, and M. Ernzerhof, Phys. Rev. Lett. **77**, 3865 (1996).

[124] S. Grimme, J. Antony, S. Ehrlich, and H. Krieg, J. Chem. Phys. **132**, 154104 (2010).

[125] S. Steiner, S. Khmelevskyi, M. Marsmann, and G. Kresse, Phys. Rev. B **93**, 224425 (2016).

[126] H. J. Monkhorst and J. D. Pack, Phys. Rev. B **13**, 5188 (1976).

[127] U. Herath, P. Tavadze, X. He, E. Bousquet, S. Singh, F. Muñoz, and A. H. Romero, Comput. Phys. Commun. **251**, 107080 (2020).

[128] H. Chen, J. Zhao, X. Wang, X. Chen, Z. Zhang, and M. Hua, Nanoscale **14**, 5551 (2022).

[129] R. E. Simon, Phys. Rev. **116**, 613 (1959).

[130] S. McDonnell, A. Azcatl, R. Addou, C. Gong, C. Battaglia, S. Chuang, K. Cho, A. Javey, and R. M. Wallace, ACS Nano **8**, 6265 (2014).

[131] S. L. Howell, D. Jariwala, C.-C. Wu, K.-S. Chen, V. K. Sangwan, J. Kang, T. J. Marks, M. C. Hersam, and L. J. Lauhon, Nano Lett. **15**, 2278 (2015).

[132] J. Fontanella, C. Andeen, and D. Schuele, J. Appl. Phys. **45**, 2852 (1974).

[133] V. K. Dugaev, P. Bruno, M. Taillefumier, B. Canals, and C. Lacroix, Phys. Rev. B **71**, 224423 (2005).

[134] T. S. Nunner, N. A. Sinitsyn, M. F. Borunda, V. K. Dugaev, A. A. Kovalev, A. Abanov, C. Timm, T. Jungwirth, J. I. Inoue, A. H. MacDonald, and J. Sinova, Phys. Rev. B **76**, 235312 (2007).

[135] T. Kato, Y. Ishikawa, H. Itoh, and J. I. Inoue, Phys. Rev. B **77**, 233404 (2008).

[136] I. A. Ado, I. A. Dmitriev, P. M. Ostrovsky, and M. Titov, Phys. Rev. Lett. **117**, 046601 (2016).

[137] S. D. Ganichev and L. E. Golub, Phys. Status Solidi B **251**, 1801 (2014).

[138] Y. Y. Tkach, Phys. Status Solidi B **258**, 2000553 (2021).

[139] M. Studer, M. P. Walser, S. Baer, H. Rusterholz, S. Schön, D. Schuh, W. Wegscheider, K. Ensslin, and G. Salis, Phys. Rev. B **82**, 235320 (2010).

[140] A. Krzyżewska and A. Dyrdał, Physica E **135**, 114961 (2022).

[141] S. D. Ganichev and W. Prettl, J. Phys.: Condens. Matter **15**, R935 (2003).

[142] S.-Q. Shen, Phys. Rev. B **70**, 081311(R) (2004).

[143] B. A. Bernevig, J. Orenstein, and S.-C. Zhang, Phys. Rev. Lett. **97**, 236601 (2006).

[144] Z. Li, F. Marsiglio, and J. P. Carbotte, Sci. Rep. **3**, 2828 (2013).

[145] X. Li, H. Tian, H. J. Zhao, C. Xu, M. Ye, L. Chen, H. Xiang, J.-M. Liu, L. Bellaiche, D. Wu, and Y. Yang, Phys. Rev. B **106**, L201105 (2022).

[146] G. Dresselhaus, Phys. Rev. **100**, 580 (1955).

[147] M. I. Dyakonov, Sov. Phys. Semicond. **20**, 110 (1986).

[148] N. S. Averkiev and L. E. Golub, Semicond. Sci. Technol. **23**, 114002 (2008).

[149] J. D. Koralek, C. P. Weber, J. Orenstein, B. A. Bernevig, S.-C. Zhang, S. Mack, and D. D. Awschalom, Nature (London) **458**, 610 (2009).

[150] L. L. Tao and E. Y. Tsymbal, Nat. Commun. **9**, 2763 (2018).

[151] H. J. Zhao, H. Nakamura, R. Arras, C. Paillard, P. Chen, J. Gosteau, X. Li, Y. Yang, and L. Bellaiche, Phys. Rev. Lett. **125**, 216405 (2020).